Molecular Therapy
Advances
Original Article

# Host determinants of exo-rAAV production revealed by extended gene expression analysis in HEK293 cells

Jesús Lavado-García,[1,5,6] Laia Bosch-Molist,[1,6] Carlos Ruiz-Ayala,[1] Inmaculada Jorge,[2,3] Jesús Vázquez,[2,3] Francesc Gòdia,[1] and Laura Cervera[1,4]

[1]Grup d'Enginyeria Cellular i Bioprocés, Departament d'Enginyeria Química, Biològica i Ambiental, Escola d'Enginyeria, Universitat Autònoma de Barcelona, Campus de Bellaterra, Cerdanyola del Vallès, 08193 Barcelona, Spain; [2]Laboratory of Cardiovascular Proteomics, Centro Nacional Investigaciones Cardiovasculares (CNIC), C/ Melchor Fernández Almagro 3, 28029 Madrid, Spain; [3]Centro de Investigación Biomédica en Red Enfermedades Cardiovasculares (CIBERCV), 28029 Madrid, Spain; [4]Serra Húnter Lecturer Professor, Barcelona, Spain

**Recombinant adeno-associated viruses (rAAVs) are leading vectors for gene therapy, yet their large-scale manufacturing remains constrained by low scalability and high costs. Here, we present an integrated systems biology and process engineering strategy to intensify rAAV production through the extended gene expression (EGE) methodology. EGE has been reported to significantly increase rAAV yields, enhanced viral egress, and promote the secretion of exosome-associated AAVs (exo-AAVs), resulting in higher extracellular titers and improved vector potency. Quantitative multiplexed proteomics revealed coordinated remodeling of host-cell pathways involved in vesicle trafficking, lipid biosynthesis, protein homeostasis, and nuclear transport. Functional validation identified key host regulators of exo-rAAV biogenesis and secretion, including CD63, VPS37B, SMPD3, and SNAP47. Targeted modulation of these pathways enabled rational enhancement of extracellular rAAV recovery in standard batch processes. Using a DoE-based mixture design, we achieved 50% viral egress into the supernatant, with >21% being exo-AAVs, demonstrating efficient translation of the EGE phenotype into scalable batch manufacturing. Collectively, this work provides a scalable and cost-effective alternative production platform with the advantages of the EGE methodology. These findings can help advance next-generation rAAV manufacturing and support the development of gene therapy vectors.**

## INTRODUCTION

Recombinant adeno-associated viruses (rAAV) have emerged as one of the vectors of choice for many gene therapy applications due to their desirable characteristics. Adeno-associated virus (AAV) vectors exhibit a high safety profile, are poorly immunogenic and have not been associated with any disease in humans.[1] rAAV vectors show robust and stable transduction efficiency in non-dividing cells, conferred by the episomal state of their DNA in the cell nucleus. Capsid engineering strategies, including rational design and directed evolution have further expanded their therapeutic potential by improving tissue targeting and enabling access to additional organs,[2–4] resulting in broad serotype-dependent tissue tropisms.

In recent years, the number of worldwide phase 1–3 clinical trials using rAAV vectors has increased to over 200, yielding promising results in terms of safety and efficacy for both monogenic disorders and genetically defined idiopathic diseases.[5,6] However, one of the main challenges facing rAAVs production is the limited scalability of transient gene expression (TGE) systems. Effective transfections can only be carried out at low cell densities, while transfection or infection at higher cell densities leads to a drastic reduction in cell-specific productivity, a phenomenon known as the cell density effect (CDE).[7] The CDE represents the principal scalability bottleneck for industrial rAAV manufacturing.[6,8] Large-scale production of rAAV vectors while maintaining high-quality in terms of purity and potency remains a major challenge, with preclinical studies often requiring $10^{15}$ to $10^{16}$ vector genomes range.[8,9]

To intensify rAAV production processes, extended gene expression (EGE) strategies based on fresh medium replacement (MR) every 48 h combined with retransfections, have been developed.[10,11] This methodology has been successfully used for rAAV9 production,

Received 12 February 2026; accepted 15 July 2026;
https://doi.org/10.1016/j.omta.2026.201815.

[5]Present address: Biotechnology Research Institute for the Green Transition (BRIGHT), Technical University of Denmark, Lyngby 2800, Denmark

[6]These authors contributed equally

**Correspondence:** Jesús Lavado-García, Grup d'Enginyeria Cellular i Bioprocés, Departament d'Enginyeria Química, Biològica i Ambiental, Escola d'Enginyeria, Universitat Autònoma de Barcelona, Campus de Bellaterra, Cerdanyola del Vallès, 08193 Barcelona, Spain.
**E-mail:** jlavgar@dtu.dk
**Correspondence:** Laura Cervera, Grup d'Enginyeria Cellular i Bioprocés, Departament d'Enginyeria Química, Biològica i Ambiental, Escola d'Enginyeria, Universitat Autònoma de Barcelona, Campus de Bellaterra, Cerdanyola del Vallès, 08193 Barcelona, Spain.
**E-mail:** laura.cervera@uab.cat


Published by Elsevier Inc. on behalf of The American Society of Gene and Cell Therapy.
This is an open access article under the CC BY-NC-ND license (http://creativecommons.org/licenses/by-nc-nd/4.0/).

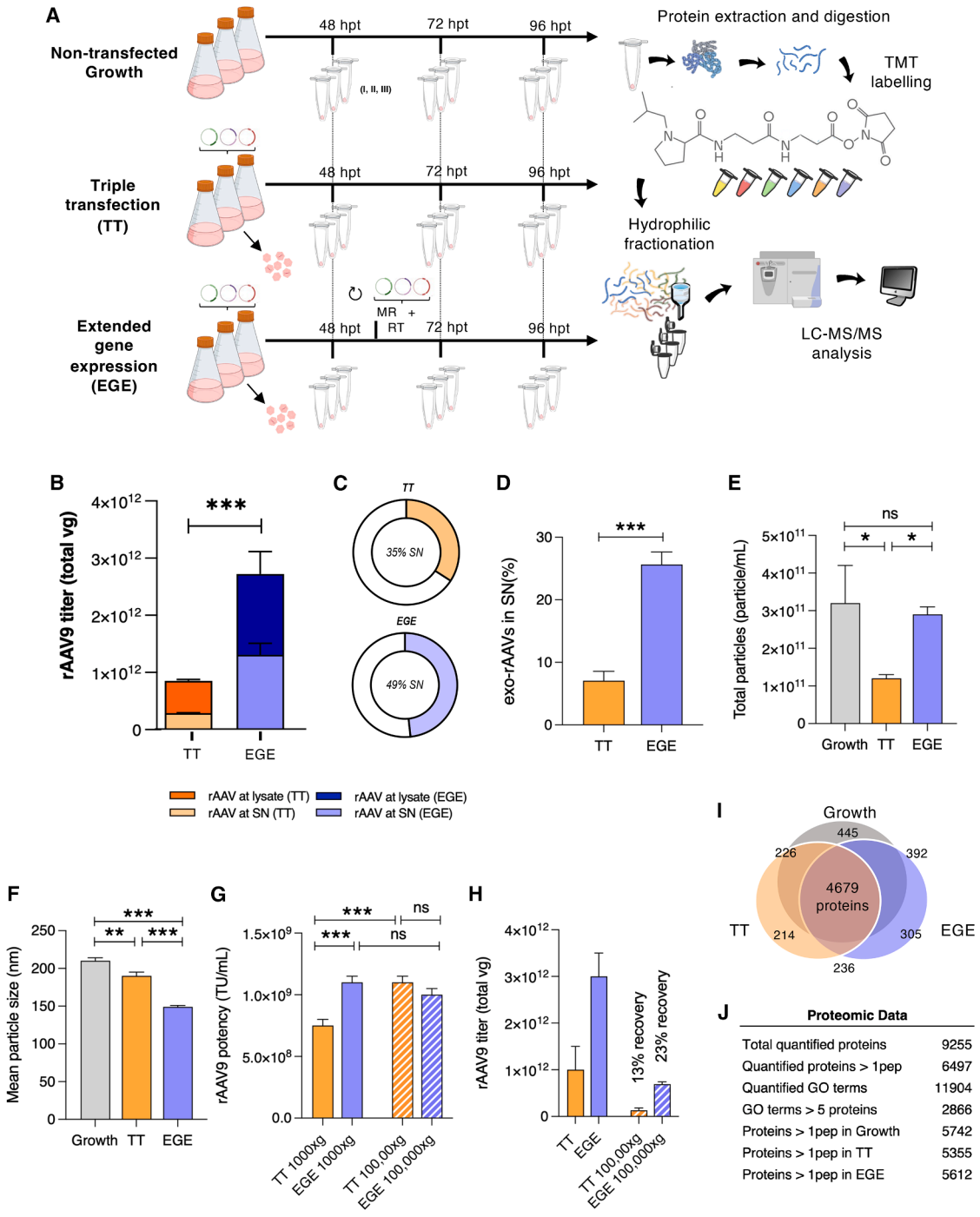



**Figure 1. Experimental design, rAAV9 production analysis, and overall proteomic data**

(A) Experimental workflow. Three biological replicates—I, II, and III of a HEK293 cell growth condition and two rAAV9 production conditions: standard triple transfection (TT) protocol and extended gene expression (EGE) protocol characterized by a medium replacement (MR) and re-transfection step at 48 h post-transfection (hpt). Cell culture samples were taken at 48, 72, and 96 hpt. Proteins were extracted from the pellet samples, digested, and peptides were labeled using tandem mass tag (TMT) labeling. Labeled peptides were fractionated and analyzed via LC-MS/MS. (B) Total cumulative rAAV9 titer in cell lysate and cell supernatant at 96 hpt from a 10 mL cell culture. (C) Fraction of total rAAV9 harvested 96 hpt accumulated in cell supernatant fraction (SN). (D) Percentage of exo-rAAVs in the rAAV titer measured in the supernatant. Free rAAVs were purified using an iodixanol gradient and exo-rAAVs following a standard exosome purification protocol. (E and F) Particle concentration and mean particle size (F) measured by NTA from the 100,000× g fraction of growth, TT, and EGE conditions. (G) Potency of collected rAAV fractions produced by TT or EGE. Potency was

*(legend continued on next page)*

achieving a 3-fold increase in the total rAAV harvested from the supernatant (SN), compared to conventional transient transfection (TT) in batch mode with cell lysate (Lys) recovery.[12] EGE enables continuous harvesting of secreted rAAVs directly from the culture SN, eliminating the need for cell lysis and facilitating downstream processing.[10,11] This approach significantly reduces host cell protein and DNA contamination, thereby improving product quality and process efficiency.[12] The implementation of perfusion-based operation has also been linked to partial modulation of the CDE by relieving metabolic burden and enabling retransfections.[13] Altogether, EGE represents a promising and scalable manufacturing strategy that preserves the flexibility of TGE while enabling compatibility with continuous large-scale production processes, positioning it as a competitive alternative to stable gene expression (SGE) platforms for rAAV manufacturing.

Interestingly, in this work, EGE implementation was observed to be associated with a marked increase in the fraction of rAAVs recovered in the SN. One of the observed elements in the SN of the EGE condition are rAAVs packaged within extracellular vesicles (EVs), referred to as exosome-associated rAAVs (exo-rAAVs). Exo-rAAVs offer multiple advantages over conventional free rAAV particles, including enhanced transduction efficiency, improved tissue penetration, and reduced susceptibility to neutralizing antibodies.[14–18] Encapsulation within EVs protects viral capsids from antibody-mediated neutralization, enabling more efficient gene delivery even in the presence of pre-existing anti-AAV immunity. Exo-rAAVs have also been shown to improve delivery across biological barriers, including the blood-brain barrier.[18] Although the content of cell-derived exosomes can promote immunogenicity toward the AAV-encoded gene,[19] *in vivo* studies demonstrate that exo-rAAVs achieve higher gene transfer efficiency in multiple tissues at lower doses than standard AAVs, thereby improving therapeutic index and reducing dose-related toxicity in some cases.[20,21] These properties position exo-rAAVs as a next-generation vector platform with significant potential for safer, more efficient, and broadly applicable gene therapy applications.

Here, a high-throughput quantitative proteomic approach was used to identify and quantify pathway-level changes associated with exo-rAAV following EGE implementation. Subsequently, rational metabolic engineering strategies were designed to bring these changes to batch mode, thereby increasing exo-rAAV productivity. Three different conditions were compared: a non-transfected HEK293 growth control, a standard TT-based rAAV production condition, and an EGE condition combining MR and re-transfection at 48 h post-transfection (hpt). The results presented here provide mechanistic insight into exo-rAAV biogenesis and enable the rational design of scalable manufacturing strategies, contributing to improved rAAV production, increased scalability, reduced downstream and production costs, higher titers, and the development of industrially relevant platforms for large-scale rAAV vector manufacturing.

## RESULTS

### Exo-rAAV secretion is improved by the EGE method

To test the individual contribution of the EGE methodology to the secretion of exosome-associated AAVs (exo-AAVs), rAAV9 titers were measured by quantitative polymerase chain reaction (qPCR) in the SN for both TT and EGE method (Figure 1A). AAV9 serotype was selected for this study because previous reports have shown that rAAV9 is efficiently released in association with EVs, making it one of the serotypes most prone to secretion and therefore a suitable model for optimizing secreted rAAV production together with its high effective rate for *in vivo* transduction.[8,22] When EGE methodology was performed, secreted rAAV significantly improved by 3.48-fold in comparison to standard transfection in both SN and total cell lysis samples (Figure 1B). The proportion of rAAV9 secreted into the SN was 49% with the EGE method, significantly higher than the 35% observed in the TT production (Figure 1C). Moreover, the percentage of exo-AAVs in the SN was 7% and 25% in the TT and in the EGE condition, respectively (Figure 1D). This indicated that the EGE protocol is associated not only with increased production titers but with enhanced efficiency of exo-rAAV9 viral egress. Moreover, the EGE method sustained cell viability at around 80%, whereas the TT protocol showed a decrease to 60% (Figure S1). To further study the association of harvested rAAV9 at cell SN with EVs, the obtained SN fraction at 96 hpt was sequentially centrifuged at 100,000× g to harvest and analyze EVs. We observed a remarkably higher particle concentration in the EGE condition, significantly higher than in the TT method (Figure 1E) with significantly smaller particle size (Figure 1F). The growth condition showed higher particle concentration compared to TT since their growth rate is higher (Figure S1A) and accumulate more EVs in batch mode. Dynamic light scattering (DLS) analyses of the SN showed a bimodal size distribution in the cell SN fraction for the TT condition with particles around 20 nm, that may correspond to rAAVs, and a prominent peak of larger EVs around 300 nm (Figure S1D). The EGE condition showed two peaks of reduced size compared to TT, one at around 30 nm and another at 100 nm that may correspond to small EVs or exosomes (Figure S1D). In the growth condition, a single peak of 35–40 nm was observed (Figure S1D). Upon ultracentrifugation at 100,000 ×g, the fraction containing EVs was analyzed by DLS (Figure S1E) showing a prominent peak from 20 to 100 nm in the EGE condition. By analyzing this fraction by dot blot, the presence of exosome markers like tetraspanins CD9, CD63, and CD81 was confirmed in the EGE condition (Figure S1F). Finally, the potency

measured from samples derived from the supernatant (1,000× g) and the pellet after ultracentrifugation (100,000× g). All experiments were run with three biological replicates ($n = 3$). Data were analyzed by one-way analysis of variance (ANOVA) for significant difference $^{*}p < 0.05$; $^{**}p < 0.01$; $^{***}p < 0.001$; error bars indicate the SD. (H) Total vg recovery after ultracentrifugation for EGE and TT conditions compared to the full lysate titer in TT and EGE. (I) Venn diagrams showing the number of proteins quantified with more than 1 peptide in each of the analyzed conditions. (J) Main proteomic data from the study. Significant Gene Ontology (GO) terms were calculated by SBT model with 5% FDR. Vg, vector genomes; TT, triple transfection; EGE, extended gene expression; MR, medium replacement; SN, supernatant; RT, re-transfection.

of the rAAV in the various collected fractions was evaluated by assessing the transduction efficiency of different rAAV9 preparations on HEK293 cells, with wild type (WT) AdV2 co-infection for signal amplification. Interestingly, this revealed that rAAVs in the SN (1,000× g) derived from the EGE method exhibited greater potency than those from TT production method when evaluated directly from the supernatant fraction (Figure 1G). In addition, following ultracentrifugation (100,000× g), rAAVs produced by both the EGE and TT methods exhibited comparable transduction efficiencies. This indicates that the intrinsic potency of rAAVs generated using the two approaches is similar. However, implementation of the EGE strategy results in a higher proportion of rAAVs being secreted into the culture SN. This observation underscored the impact of enriching EV content on rAAV potency, due to enhanced secreted rAAV recovery. Moreover, the EGE method demonstrated a superior recovery efficiency of rAAV particles after ultracentrifugation, with 23% of vector genome titer (vg) recovered compared to 13% using the TT method (Figure 1H). This suggests a higher association of rAAVs with EV particles in the EGE SN compared to TT, leading to more efficient recovery. This finding emphasizes the effectiveness of the EGE method in enhancing rAAV yield and potency through improved EV association. To further unveil the changes in secretion pathways leading to these results, the proteome of the different conditions was analyzed. The final objective was to transfer the high exo-rAAV9 secretion phenotype observed under EGE conditions to batch mode in order to intensify the production process.

### Proteomic landscape upon rAAV production

Altered cellular processes upon TT and EGE implementation during rAAV production were identified using a multiplexed quantitative proteomic approach. Individual proteins were quantified showing differential protein changes in each studied condition. A total of 9,255 proteins were identified and quantified in this study. From these, 6,497 proteins were quantified with more than one peptide. From these 6,497 proteins, 4,679 were present in all three conditions, accounting for 81.5%, 87.4%, and 83.4% of proteins from non-transfected, TT, and EGE conditions, respectively (Figures 1I and 1J). All analyses, except if specifically mentioned, were carried out using this set of 4,679 common proteins. However, some proteins were exclusively identified in one or two conditions. Coherently, AAV-composing proteins such as Rep78, Rep68, and the capsid proteins VP1, VP2, and VP3 were only identified in the TT and EGE conditions (Table S1). E1a and E1b proteins were also identified in the control non-transfected condition (Table S1) as they are constitutively expressed in HEK293 cells. Interestingly, expression of E1a was downregulated in the TT condition at 96 hpt. From the 236 proteins that presented up- or downregulation and were quantified only in TT and EGE conditions, apart from the AAV-composing proteins, versican core was significantly upregulated (false discovery rate [FDR]<0.05) at 72 and 96 pht in TT and at 96 hpt in EGE condition (Table S1). From the protein analysis using the Systems Biology Triangle (SBT) method of biological process enrichment, 11,904 Gene Ontology (GO) terms or categories were quantified, from which 2,866 were quantified with more than 5 proteins (Figure 1J). The main altered biological processes in the EGE condition were analyzed aiming to understand how the EGE methodology influenced the exo-rAAV production process. Significantly (FDR<0.05) up- and downregulated GO biological process terms in EGE condition were analyzed showing that processes related to viral transcription and protein biosynthesis, such as translational initiation, protein binding, and stabilization were upregulated while processes involved in DNA repair and cell cycle were downregulated at all time points. As previously reported, cell cycle and proliferation significantly decreased upon polyethylenimine (PEI)-mediated TT.[23] Furthermore, more than 40 biological processes GO terms related to cell cycle and DNA repair such as G1/S transition of mitotic cell cycle, regulation of cell cycle, G2 damage checkpoint and DNA binding were downregulated in TT and EGE conditions. Interestingly, the expression of proteins involved in the formation of the DNA repair MRN complex such as Rad50 and MRE11 were observed to be significantly downregulated upon AAV production (Table S1). The downregulation of this complex has been reported to enhance replication of AAVs.[24,25]

### Study of the different vesicle transport pathways upon rAAV production

Based on the increase of exo-rAAVs generation upon implementation of the EGE protocol (Figure 1D), biological processes and proteins that significantly changed in EGE condition related to vesicle transport were analyzed. 17 biological process GO terms related to vesicle transport were upregulated upon rAAV production These processes were not only upregulated in TT and EGE condition compared to the control non-transfected condition, but they also were upregulated in EGE compared to TT condition (Figures 2A–2C). Protein families involved in aggregation and cargo transport such as CCT and COP proteins were all upregulated in TT and EGE conditions (Table S1), indicating an increase in EV production upon PEI-mediated TT, as previously reported.[26] Interestingly, most exosome markers showed a downregulation in EGE condition except for tetraspanin CD63 (Figure 2B; Table S1).

Exosome secretion requires the biogenesis of multivesicular bodies (MVBs) and fusion of MVB with the cell membrane. The loading of cargo into MVB has been reported to follow multiple pathways. At least three different routes have been described: the ESCRT pathway, the tetraspanin pathway, and a route involving lipids such as sphingomyelin.[27] Regarding the ESCRT pathway, in our study, proteins from ESCRT-II and ESCRT-III did not show significant differences in EGE condition. ESCRT-0 was significantly downregulated in EGE so it was not further evaluated. ESCRT-I protein VPS37B showed a significant increase in EGE at 96 hpt, thus indicating a role for ESCRT-I on rAAV secretion. To validate this possible pathway interaction, two plasmids encoding a small hairpin RNA (shRNA) targeting VPS37B gene were evaluated since VPS37B depletion has been previously reported to lead to ESCRT-I destabilization.[28] Tetraspanins have also been described as proteins influencing loading of MVB. In our study, only CD63 was observed to report a significant change in EGE condition. In this condition, CD63 was upregulated compared to non-transfected and to standard

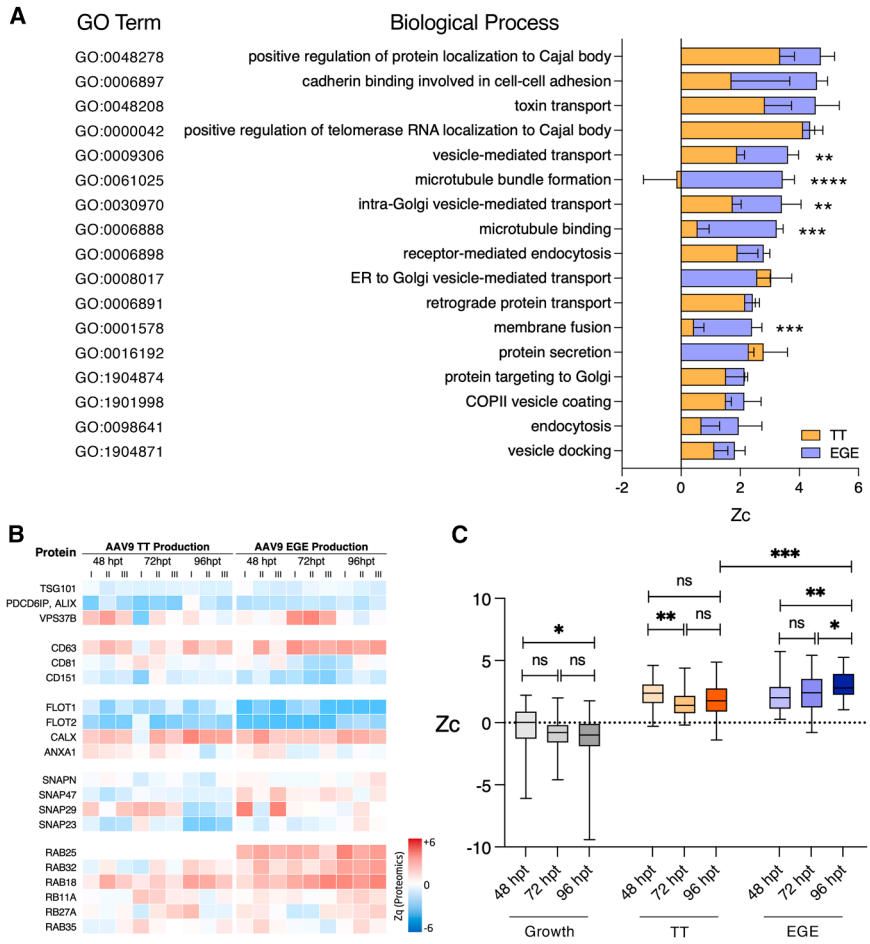



**Figure 2. Proteomic data regarding vesicle transport**

(A) Gene Ontology (GO) biological processes terms regarding vesicle transport, quantified with more than 5 proteins by SBT model with 5% FDR at 96 hpt. Zc values are represented in orange for standard triple transfection (TT) and purple for extended gene expression (EGE) production. (B) Heatmap of some representative quantified proteins involved in vesicle transport. Zq values are represented in red for upregulation and blue for downregulation. I, II, and III—three biological replicates. (C) Boxplots representations of the Zc values from the vesicle transport GO terms. Medians are represented by horizontal bars and whiskers extend to extreme data points. Significance was calculated using one-way ANOVA and Tukey tests. $*p < 0.05$; $**p < 0.01$; $***p < 0.001$, $****p < 0.0001$.

production condition. Another route for loading the MVB with cargo to be later released in the form of exosomes is via ESCRT-independent and tetraspanin-independent pathways like the one triggered by the metabolization of ceramide.[29] The expression of sphingomyelinase or sphingomyelin phosphodiesterase enzymes breaking down sphingomyelin to ceramide has been reported to contribute to the pathways sorting cargo into the different routes within the MVB, overexpressed in EGE condition (Figure 3). The second step in exosome generation is the fusion of the MVB to the cell membrane, releasing its cargo to the extracellular medium. Regarding the regulation of this step, the families of Rab and SNAP proteins have been reported to be heavily involved.[27,30,31] From more than 46 different quantified Rab proteins (Table S1), Rab25, Rab32, and Rab18 showed upregulation in EGE condition (Figure 2B). From these three Rab proteins, Rab32 was identified with the highest number of proteotypic peptides (Table S1). Among SNAP proteins, SNAP47 showed the highest upregulation in EGE compared to TT and non-transfected conditions (Figure 2B).

### Effects of rAAV production on lipid biosynthesis

Biological processes related to lipid biosynthesis were downregulated along cell growth in the control non-transfected condition in agreement to previous reported work.[23] Conversely, these GO terms were upregulated in TT and EGE conditions (Figures 3A–3C). Moreover, within EGE condition, lipid biosynthesis was significantly upregulated along the time course, increasing at 72 and 96 hpt (Figure 3C). Specifically, the biosynthesis of fatty acids, lipids, and cholesterol showed a similar upregulation trend while glycosphingolipid metabolism was significantly downregulated on both rAAV production methods. Enzymes involved in glucosylceramide hydrolysis such as glucosylceramidases and prosaposin were heavily downregulated in the EGE condition (Table S1) suggesting that glycosphingolipid metabolism might play a role in exo-rAAV secretion to the extracellular medium, since adding ceramide to the TT condition substantially reduced extracellular rAAV production (Figure 4A).

### Modulation of secretion pathways increases extracellular rAAV production and viral egress rate

Based on the proteomic alterations in vesicle trafficking and lipid biosynthesis observed under the EGE condition (Table S1), we next selected targets related to exo-AAV production pathways and were upregulated in the EGE condition compared to TT. We evaluated whether targeted modulation of the identified candidate exo-rAAV regulators, such as CD63, VPS37B, SNAP47, Rab32, and SMPD3 could enhance exo-rAAV production in batch mode. This approach aimed both to translate the EGE-associated molecular signatures into standard batch processes and to causally validate whether the proteomic changes observed under EGE were directly linked to exo-rAAV secretion.

Overexpression of CD63, VPS37B, SNAP47, and SMPD3 led to a significant increase in rAAV titers in the culture SN, with the largest effect observed for SNAP47, followed by VPS37B. Although specific

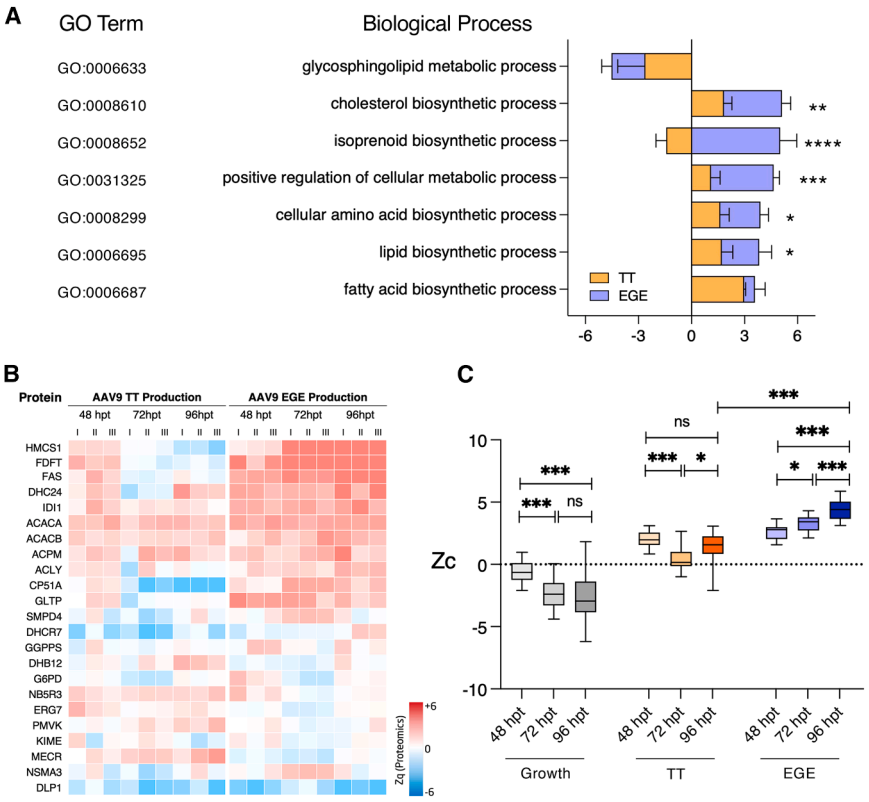



**Figure 3. Proteomic data regarding lipid and glycosphingolipid metabolism**

(A) Gene Ontology (GO) biological processes terms regarding vesicle transport, quantified with more than 5 proteins by SBT model with 5% FDR at 96 hpt. Zc values are represented in orange for standard triple transfection (TT) and purple for extended gene expression (EGE) production. (B) Heatmap of some representative quantified proteins involved in lipid and glycosphingolipid metabolism. Zq values are represented in red for upregulation and blue for downregulation. Three biological replicates—I, II, and III. (C) Boxplots representations of the Zc values from the lipid and glycosphingolipid metabolism GO terms. Medians are represented by horizontal bars and whiskers extend to extreme data points. Significance was calculated using one-way ANOVA and Tukey tests. $*p < 0.05$; $**p < 0.01$; $***p < 0.001$, $****p < 0.0001$.

Rab GTPases have been reported to interact with exosome biogenesis and regulation pathway,[31] overexpressing Rab32 did not lead to a significant increase in rAAV titers compared to TT control (Figure 4A).

DLS analysis of particle size distributions showed that CD63 overexpression produced a particle profile highly comparable to that observed in the control TT production, characterized by a primary peak at 50–60 nm and a secondary peak at ∼400 nm (Figure 4B). In contrast, the DLS profiles obtained upon Rab32 and SNAP47 overexpression differed from both the TT production and the growth control conditions. In both cases, the particle distributions exhibited a dominant peak around 250 nm, with the SNAP47 condition showing a higher proportion of total particle volume within this peak (Figure 4B). For SMPD3 overexpression, the DLS particle size distribution closely resembled the profile observed for the TT production condition (Figure 4B).

To further investigate the role of SMPD3, ceramide was added to both the control TT production and the SMPD3-overexpressing condition. Ceramide supplementation significantly reduced extracellular rAAV titers compared with both the TT production and the SMPD3 overexpression conditions (Figure 4A). Interestingly, upon ceramide addition, the DLS particle size distribution shifted away from the TT control profile and became comparable to the growth control condition, in which no rAAV production occurs (Figure 4B).

To further evaluate whether CD63 and VPS37B are directly involved in rAAV secretion, we performed complementary loss-of-function experiments using shRNA-mediated knockdown during TT. This approach allowed us to assess whether reducing the expression of these candidate genes would result in decreased rAAV release to the culture SN. Silencing VPS37B using shRNA constructs (pshVPS37B.1 and pshVPS37B.2) resulted in a significant decrease in rAAV titers in the culture SN compared with both the standard TT production and the scrambled shRNA control (pshScramble) (Figure 4C). Similarly, co-transfection with a plasmid encoding an shRNA targeting CD63 (pshCD63) led to a significant reduction in extracellular rAAV titers, following a pattern comparable to that observed for VPS37B-targeting shRNAs (Figure 4C). Consistent with these results, the corresponding DLS particle size distribution profiles showed a marked shift relative to the TT production condition. In particular, CD63 knockdown resulted in a dominant peak at approximately 25 nm, distinct from the particle profile observed during standard rAAV production (Figure 4D). Together, these findings support a role for both CD63 and VPS37B in rAAV secretion and egress to the extracellular medium.

Following the observations that rAAV titers in the cell SN fraction were influenced by the identified proteins targeting the EV pathway, further experiments were conducted to assess the TT impact of protein combinations on rAAV9 secretion. Specifically, the effects of co-expressing two proteins and rAAV9 titer in the cell SN fraction were characterized. Combinations of CD63, SMPD3, VPS37B, and SNAP47 transient overexpression were included in the TT batch process. These combinations also contributed to increase rAAV secretion

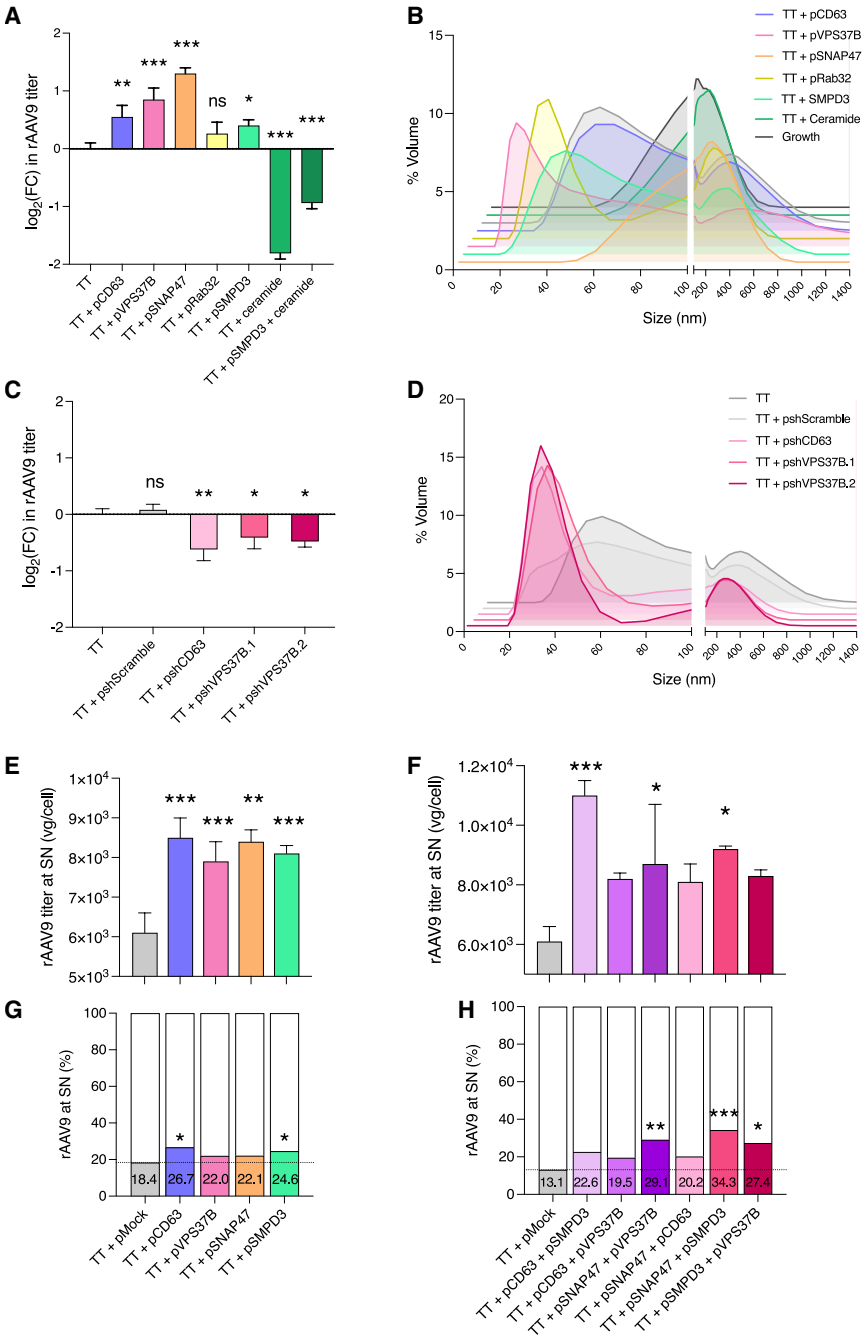



**Figure 4. Characterization of rAAV9 titer and produced exo-AAVs**

(A) rAAV9 titer expressed as $log_2$FC (fold change) of standard triple transfection plasmids (TT) adding a different test plasmid harboring a shRNA targeting different genes in each condition compared to standard triple transfection with pMock. (B) Comparison of DLS plot between the different shRNA generated in co-transfection with TT plasmids. (C) rAAV9 titer expressed as $log_2$FC (fold change) of standard triple transfection plasmids (TT) adding a different test plasmid overexpressing different genes in each condition compared to standard triple transfection with pMock. (D) DLS plot of TT adding different tested plasmids, showing different volume of extracellular vesicles at different size at the supernatant. (E) rAAV9 titer in the supernatant (SN) of quadruple transfection using standard triple transfection (TT) plasmids adding one of the candidate genes. Color coding represents the studied condition coded below. (F) rAAV9 titer of triple transfection plasmids co-transfected with two candidate genes. Color coding represents the studied condition coded below. (G and H) Percentage of rAAV9 found at the supernatant (SN). The dotted line represents the value for the TT + pMock control. All experiments were run with three biological replicates. All data were analyzed by ANOVA and Dunnett test for significant difference $^*p < 0.05$; $^{**}p < 0.01$; $^{***}p < 0.001$.

to the extracellular medium, being the combination of CD63 with SMPD3 overexpression the one providing the highest fold change in rAAV titer compared to TT (Figure 4F). Additionally, the combinations of SNAP47 with SMPD3, and SNAP47 with VPS37B, also enhanced extracellular rAAV titers, although to a lesser extent.

Furthermore, rAAV egress under these conditions was evaluated (Figures 4G and 4H). When comparing individual expression of each candidate protein during TT, CD63 showed the highest percentage of rAAV9 in the cell SN fraction (Figure 4G). Among the protein combinations, SNAP47-VPS37B, SNAP47-SMPD3, and SMPD3-VPS37B showed the most pronounced rAAV egress rates (Figure 4H). As a critical parameter for the quality of the final product, the full vs. empty capsid ratio was analyzed. No significant differences among individual gene overexpression were observed (Table S2). TT control transfection reached 13.1% of full rAAV particles secreted at the extracellular medium. Overexpression of SNAP47 did not alter rAAV packaging capacity, observing a 13.57% of full rAAV particles. This led to an absolute 5.3-fold increase of full rAAV due to the overall production improvement caused by SNAP47 overexpression.

### Mixture design to optimize extracellular exo-rAAV harvest in batch mode

Having observed that SNAP47, SMPD3, and VPS37B contributed positively to rAAV yield in the SN, efforts were directed toward identifying the optimal combination of these genes to maximize rAAV

**Table 1. Mixture Design experimental matrix, results, and ANOVA analyses for the optimization of the transient overexpression of SNAP47, SMPD3, and VPS37B**

| Variables | | | | Responses | |
|---|---|---|---|---|---|
| Experimental run | pSNAP74 (%) | pSMPD3 (%) | pVPS37B (%) | Esn (%) | $q_p$ ($vg \cdot cell^{-1} \cdot day^{-1}$) |
| 1 | 0 | 0.5 | 0.5 | 51.68 | 3,575.82 |
| 2 | 0.16 | 0.16 | 0.66 | 29.40 | 4,903.38 |
| 3 | 0.5 | 0.5 | 0 | 17.13 | 11,745.95 |
| 4 | 0 | 1 | 0 | 18.14 | 13,865.20 |
| 5 | 0 | 0 | 1 | 40.58 | 3,970.19 |
| 6 | 0.66 | 0.16 | 0.16 | 37.84 | 4,024.09 |
| 7 | 1 | 0 | 0 | 22.30 | 7,938.26 |
| 8 | 0.5 | 0 | 0.5 | 21.79 | 7,666.83 |
| 9 | 0.33 | 0.33 | 0.33 | 21.06 | 9,600.76 |
| 10 | 0 | 1 | 0 | 20.48 | 11,800.18 |
| 11 | 0 | 0 | 1 | 29.21 | 7,196.95 |
| 12 | 0.5 | 0.5 | 0 | 16.55 | 13,150.01 |
| 13 | 0.16 | 0.66 | 0.16 | 24.23 | 8,033.15 |
| 14 | 1 | 0 | 0 | 30.92 | 5,398.60 |

| Model | Multiple $R^2$ | *p value*[a] | Lack of fit[b] |
|---|---|---|---|
| Esn (%) | 0.7992 | 0.0113 | 0.2183 |
| $q_p$ ($vg \cdot cell^{-1} \cdot day^{-1}$) | 0.7421 | 0.0283 | 0.1898 |

| Parameters | | | | |
|---|---|---|---|---|
| | Esn (%) | | $q_p$ ($vg \cdot cell^{-1} \cdot day^{-1}$) | |
| | Coefficient | *p value*[b] | Coefficient | *P value*[b] |
| pSNAP47 | 27.49 | 0.0243 | 6,737.61 | 0.0267 |
| pSMPD3 | 20.79 | 0.0183 | 12,230.43 | 0.0135 |
| pVPS37B | 35.12 | 0.0244 | 5,708.34 | 0.0217 |
| pSNAP47 × pSMPD3 | −26.34 | 0.1972 | 9,458.03 | 0.2412 |
| pSNAP47 × pVPS37B | −51.28 | 0.0517 | 6,796.04 | 0.4697 |
| pSMPD3 × pVPS37B | 84.10 | 0.0057 | −25,925.21 | 0.0201 |

[a]*p values* under 0.05 are considered statistically significant with 95 % confidence, and *p values* under 0.1 are considered statistically significant with 90 %.
[b]*p values* associated to lack of fit test above 0.05 mean that the hypothesis arguing that the model is suitable cannot be rejected.

egress rate. A mixture design (MD) was used to optimize the plasmid ratio for transient overexpression of the three genes, analyzing the egress rate (Equation 3) and the specific productivity (Equation 5) as responses. The experimental design matrix, response, and statistical analysis are shown in Table1. Data were fitted to a quadratic second-order polynomial equation (Equation 6). Regression analysis for both responses showed that the model fitted the data with a coefficient $R^2$ of 0.7992 and 0.7421, respectively. Further, the statistical significance of the model was confirmed by ANOVA analysis. The Fisher's $F$ test associated $p$ value of 0.0113 and 0.0283 indicated that both models were significant. Values of the linear mixture were significant, while the combination of SMPD3 and VPS37B was the only significant one in both models (Table 1). These models were used to find the optimal plasmid ratio for exo-rAAV production through contour plots (Figure 5). The experimental space is shown as a triangle and each vertex represents a formulation with 100% of one component, edges represent binary mixtures and interior points represent ternary mixtures in various proportions. The maximal egress of rAAV9 was achieved when SMPD3 and VPS37B ware combined at ratios of 0.415 and 0.585, respectively achieving a 50% egress rate (Figure 5A). The specific productivity of rAAV9 in the cell Lys was maximal when SMPD3 and SNAP47 were combined at ratios of 0.79 and 0.21, respectively achieving $1.26 \times 10^4$ vg/cell (Figure 5B). The inclusion of VPS37B had minimal influence on the specific productivity. When maximizing both combined responses, SMPD3 and VPS37 at 0.877 and 0.123 ratio led to a 31.6% of viral particles at SN and 8,631.65 vg/cell at cell Lys fraction. These optimal values were validated in triplicates and a control condition was employed where pMock was added at a concentration of $9 \times 10^{10}$ copies/mL instead of the tested plasmid combination. The viral egress rate in this condition was 19.7%, and the specific productivity 5,922.46 vg/cell. Thereby, demonstrating that the optimal

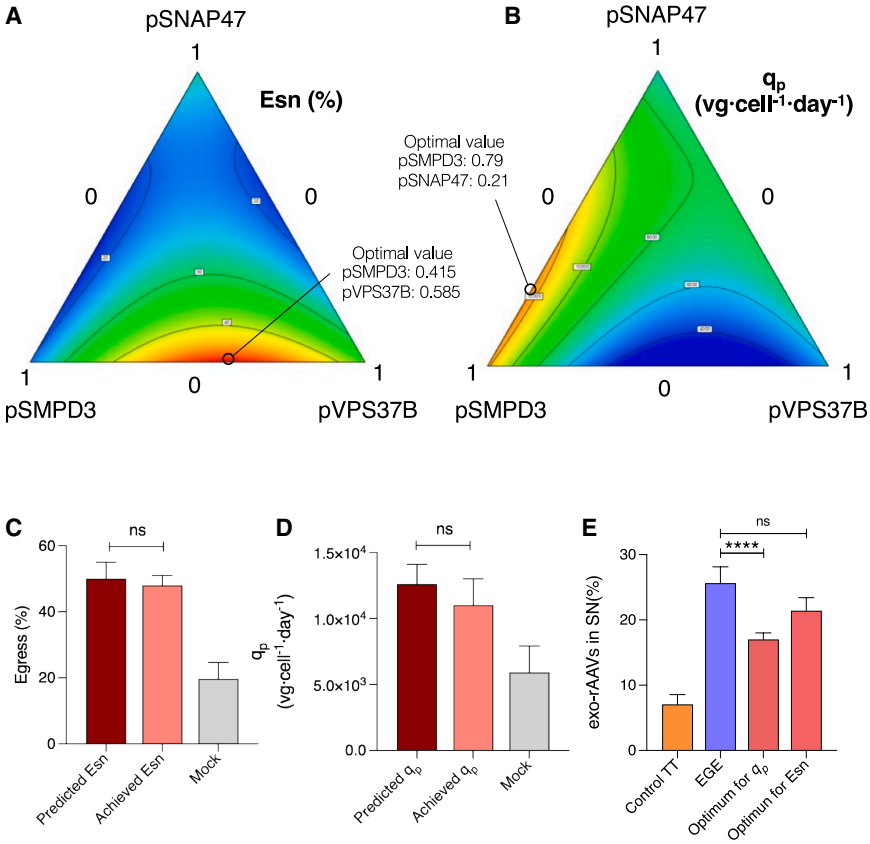



**Figure 5. Mixture Design for the optimization of secreted rAAV secretion**

(A) Contour plot for rAAV9 egress (Esn) measured as the percentage of rAAV9 detected at cell supernatant. (B) Contour plot for specific productivity response measured as total rAAV9 · cell$^{-1}$ · day$^{-1}$ at cell lysate fraction, involving cell pellet and cell supernatant. Each axis of the triangle represents one of the three plasmids (pSNAP47, PMPD3, pVPS37B) at varying concentrations, demonstrating their proportional effects on each response. The color gradient and the contour lines provide a visual representation of response variable levels, with warmer colors indicating higher values in each response. For Esn the range goes from 16.55% to 50.4% and for $q_p$ from 3,575 to 13,865 vg · cell$^{-1}$ · day$^{-1}$. (C) Validations for Esn model, showing the optimal value predicted by the model, the achieved experimental value and the value for the mock control. (D) Validations for $q_p$ model, showing the optimal value predicted by the model, the achieved experimental value and the value for the mock control. (E) Percentage of exo-rAAVs in the supernatant in TT, EGE and both optimal conditions from the MD.

plasmid combination derived from the MD outperformed the control condition for both responses (Figures 5C and 5D). Furthermore, the percentage of exo-rAAVs in the supernatant observed in the EGE condition was successfully achieved in batch mode using the optimal ratio of SMPD3 and VPS37B, significantly higher than both the TT control and the value obtained for the optimal ratio of SMPD3 and SNAP47, designed to optimize productivity but nor viral egress.

## DISCUSSION

The central objective of this study was to translate the enhanced exo-rAAV secretion phenotype observed under the EGE methodology into a standard batch production format, enabling process intensification without relying on media replacement (MR), re-transfection, or perfusion-based operations. Cryo-transmission electron microscopy (Cryo-TEM) analysis performed directly on unprocessed SN from the EGE condition (Figure 6A) confirmed the presence of vesicular structures containing rAAV particles, supporting the formation of exo-rAAVs, while routine expectation maximization (EM) analysis of the batch SN did not show presence of vesicle-associated rAAVs. By leveraging the biological insight coming from the proteomic study of EGE, we aimed to develop a simpler, scalable, and industrially relevant batch strategy that achieves higher secreted rAAV yields, reduced process time, lower media consumption, and decreased manufacturing costs, key parameters for economically viable large-scale rAAV production. Functional validation through targeted modulation of the identified pathways demonstrated that host-directed engineering alone is sufficient to achieve the rAAV secretion phenotype observed in EGE, establishing a causal rather than correlative relationship between the identified proteins and enhanced viral egress. Importantly, subsequent design of experiments (DoE)-based MD optimization enabled rational tuning of combinatorial host factor expression, resulting in extracellular recovery of more than 50% of total rAAV titers and >21% in exo-rAAVs in batch mode, representing a substantial shift from intracellular retention to extracellular secretion (Figure 6B).

Interestingly, a shift in size of produced EVs toward <200 nm vesicles has been previously reported to be triggered only by PEI-mediated transfection.[26] This increase in exosome production only by effects of transfection has been reported as a cell mechanism to excrete large amounts of DNA.[32] The fact that replacing culture media enhanced the exosome secretory pathway represents an effective method to increase exo-rAAV production with a simple operational modification at large scale. However, in order to translate the exo-rAAV phenotype observed in EGE to batch mode, it was required to understand the altered pathways triggering the increase in secreted rAAVs. These findings are significant not only from a bioprocessing perspective but also from a vector biology perspective. Mechanistically, they provide insight into rAAV egress routes and EV-mediated export mechanisms, demonstrating that rAAV secretion can be actively regulated through host pathway engineering rather than being treated as a passive byproduct of cell lysis-based recovery strategies.

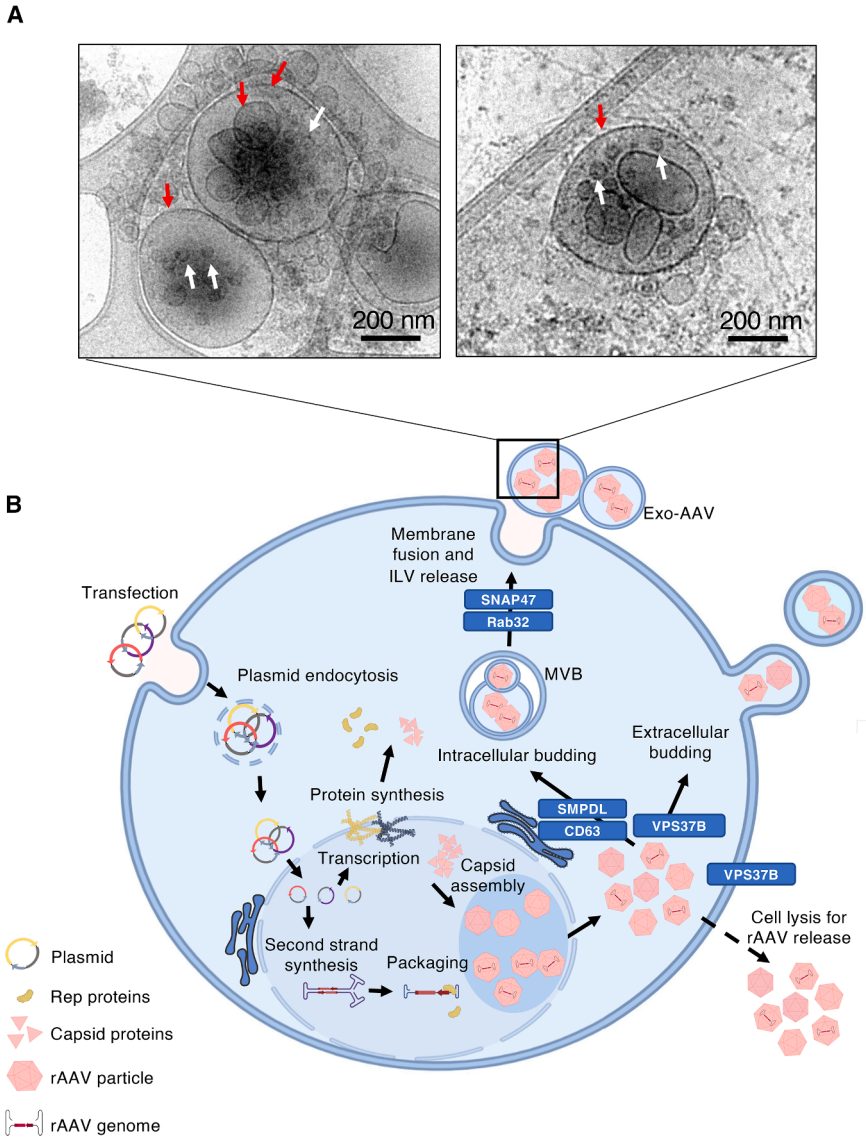



**Figure 6. Schematic representation of the pathways for rAAV and exo-AAVs synthesis and release**

(A) Cryo-transmission electron microscopy of harvested supernatant of condition TT + CD63 at 72 hpt. White arrows indicate rAAV particles and red arrows indicate exosome membranes. Image show rAAV particles associated to exosomes in supernatant fraction at harvest. (B) Pathway representation of rAAV production in EGE condition. In standard triple transfection method, rAAV particles are collected by cell lysis procedure. A fraction of rAAV vectors can be collected from the supernatant fraction as they are naturally released into the cell culture media associated with exosomes (exo-AAV). Identified proteins SNAP47 and Rab32 are involved in exosome fusion and release. SMPDL, CD63, and Vps37B participate in intracellular budding process. MVB, multivesicular bodies; ILV, intraluminal vesicles.

From a manufacturing perspective, this work explores rAAV process intensification, where vector productivity and harvest efficiency are improved through secretion engineering rather than scale-up alone. This approach enables higher yields in shorter production times with simplified downstream processing, reduced contamination burden, and improved product consistency. Moreover, enriching exo-rAAV fractions inherently enhances vector performance characteristics, including transduction efficiency and immune evasion, further strengthening the therapeutic value of the produced vectors.

Importantly, these results align with and extend existing literature supporting the role of EV pathways in rAAV secretion. For example, Schiller et al. demonstrated that overexpression of CD9 enhances the secretion of rAAV in the form of exo-AAVs, confirming the functional relevance of tetraspanin-mediated vesicle pathways in vector export.[33] In contrast to single-target strategies, the present study adopts a systems-level, proteomics-guided approach, identifying and exploiting multiple secretion pathways simultaneously. The targets selected here emerged directly from the EGE-associated proteomic landscape, enabling discovery of previously unexploited regulatory nodes such as VPS37B, SMPD3, and SNAP47 as key modulators of exo-rAAV secretion.

However, beyond vesicle trafficking and lipid metabolism, the EGE condition was associated with coordinated changes in translation, endoplasmic reticulum (ER) function, unfolded protein response (UPR) signaling, mitochondrial metabolism, nuclear import machinery, and cell cycle regulation (Figures S2–S4), indicating the establishment of a distinct host cell state optimized for sustained vector biosynthesis and secretion. These findings support the view that improved rAAV production arises from systems-level host adaptation, rather than modulation of a single pathway, motivating a broader analysis of the cellular mechanisms underlying enhanced productivity and scalability.

Regarding protein homeostasis, the dominant host response was characterized by disruption of proteostasis and induction of ER stress, particularly under standard TT conditions. This was evidenced by activation of UPR pathways, including PERK and ATF6 signaling, and upregulation of protein folding and refolding processes, consistent with previous reports in HEK293-based rAAV systems.[34–36] In contrast, the EGE method induced distinct metabolic adaptations that appear to mitigate ER stress and restore proteostatic balance. These included increased expression of ubiquitin-proteasome system components, enhanced cytoplasmic chaperone activity (e.g., HSPA1), and reduced reliance on ER-resident chaperones such

as calreticulin, suggesting a redistribution of protein quality control mechanisms toward more efficient cytoplasmic folding and degradation. Collectively, these changes indicate that EGE promotes a cellular state with a less pronounced UPR, improved protein homeostasis, and greater cellular resilience, which likely contributes to the higher viability and productivity observed during rAAV production.

Regarding cell cycle regulation, it is driven by the coordinated actions of viral proteins supplied by both helper plasmids and the HEK293 genome. These viral factors exert opposing regulatory effects, with adenoviral E1A promoting G1/S transition through pRb inhibition and E2F activation, while Rep78 induces antiproliferative responses and S-phase arrest, creating a tightly controlled cellular state that favors viral replication.[37,38] Proteomic analysis revealed that TT disrupts normal cell cycle progression, particularly impairing G1/S transition and mitotic checkpoint regulation (Figure S4). In contrast, the EGE protocol partially restores cell cycle dynamics by reducing negative regulators of the G1/S transition, promoting S-phase entry, and enhancing G2/M progression. These changes are consistent with the known requirement for S/G2-phase environments to support AAV genome replication and viral production. Mechanistically, EGE-associated upregulation of ubiquitin-proteasome pathways and lipid biosynthesis suggests accelerated turnover of cell cycle regulators and membrane remodeling required for mitotic progression. Collectively, these adaptations indicate that EGE reprograms cell cycle control toward a more permissive, production-competent cellular state, providing a mechanistic basis for its superior productivity and highlighting cell cycle modulation as a rational target for future rAAV process intensification strategies.

The EGE phenotype also appears to mitigate key features of the CDE, which is known to limit cell-specific productivity at high cell densities through metabolic and transport constraints. CDE is typically associated with suppression of lipid biosynthesis and reduced expression of nuclear transport machinery.[23] However, EGE induces the opposite profile. Notably, lipid biosynthetic pathways are upregulated under EGE, including enzymes such as HMGCS1, supporting membrane biogenesis and cellular energetics required for sustained productivity. In parallel, while cellular importins are downregulated under high cell density conditions,[23] the EGE protocol reverses this effect, prominently upregulating KPNA2 (importin α2), a key nuclear pore complex component that mediates canonical importin α/β-dependent nuclear transport.[39] Given that rAAV capsid nuclear entry relies on this pathway via VP1 nuclear localization signal (NLS) recognition,[40] enhanced importin expression under EGE likely facilitates increased nuclear availability of capsid proteins, thereby alleviating packaging limitations. Together, these metabolic and transport adaptations indicate that EGE not only enhances exo-rAAV secretion but also functionally counteracts core CDE mechanisms.

Metabolic engineering of the EV pathway revealed distinct and complementary strategies for enhancing exo-rAAV production and viral egress. CD63 overexpression not only increased rAAV titers in the SN but also significantly promoted EV co-production, suggesting an enrichment in exo-rAAVs. Overexpression of CD63 likely promotes the enrichment of exo-rAAVs by enhancing the biogenesis and trafficking of intraluminal vesicles within the endosomal system. CD63 is a tetraspanin highly enriched in late endosomes and MVBs, where it plays a key role in exosome formation and cargo sorting. Increased CD63 expression has been associated with enhanced exosome secretion and modulation of vesicle composition, potentially facilitating the incorporation of viral particles into these vesicular structures.[41,42] In the context of rAAV, previous studies have shown that a fraction of viral particles can associate with EVs during egress, thereby contributing to the formation of exo-rAAVs.[16,43] Therefore, CD63 overexpression may increase the availability of MVB-derived vesicles and promote rAAV packaging into these compartments, ultimately enhancing their release in association with exosomes. This dual effect suggests that a CD63-overexpressing stable HEK293 cell line could represent a powerful manufacturing platform, enabling sustained exo-rAAV production under standard TT conditions. This concept is supported by previous work using CD9-overexpressing HEK293 cells, which increased exo-rAAV generation but did not improve total extracellular rAAV titers,[33] highlighting CD63 as a more effective target for simultaneously enhancing both EV biogenesis and viral secretion. Such a platform would facilitate exploitation of the unique therapeutic properties of exo-rAAVs, including surface engineering with ligands or receptors to expand tissue tropism, while also motivating the development of scalable purification strategies beyond ultracentrifugation, such as chromatography-based processes compatible with industrial manufacturing.

Overexpression of VPS37B likely enhances rAAV secretion by modulating the ESCRT-I complex, a key regulator of endosomal sorting and MVB formation. VPS37B is a core component of ESCRT-I, which is involved in membrane deformation and intraluminal vesicle budding within MVBs, processes that underpin exosome biogenesis and cargo incorporation.[44,45] Increased expression of VPS37B may therefore promote vesicle formation and trafficking through the endosomal pathway, facilitating the sorting and release of rAAV particles via EVs. Consistent with this, ESCRT machinery has been implicated in the budding and egress of multiple enveloped and non-enveloped viruses, as well as in EV-mediated transport mechanisms.[46] In this context, VPS37B overexpression may enhance the coupling between rAAV trafficking and vesicular export pathways, contributing to increased extracellular rAAV levels, including vesicle-associated forms.

Likewise, overexpression of SNAP47 may enhance rAAV secretion by facilitating SNARE-mediated vesicle fusion processes involved in intracellular trafficking and exocytosis. SNAP47 is a member of the SNAP family of t-SNARE proteins that participate in membrane fusion events, including vesicle docking and release at the plasma membrane and along the endosomal pathway.[47,48] Increased SNAP47 expression could promote the fusion of vesicle intermediates, such as MVBs or recycling endosomes, with the plasma membrane, thereby enhancing the release of vesicle-associated cargo, including rAAV particles. In line with this, SNARE proteins have been

implicated in the secretion of EVs and in viral egress pathways that rely on host membrane trafficking machinery.[42] Therefore, SNAP47 overexpression may increase the efficiency of vesicular transport and fusion steps required for rAAV export, contributing to elevated extracellular titers and potentially vesicle-associated rAAV release.

On the other hand, overexpression of SMPD3 may influence rAAV secretion by regulating ceramide-dependent membrane remodeling and EV biogenesis. SMPD3 catalyzes the hydrolysis of sphingomyelin to ceramide, a lipid that promotes negative membrane curvature and facilitates inward budding of endosomal membranes during MVB formation.[29,49] This ceramide-driven pathway represents an ESCRT-independent mechanism of exosome biogenesis and has been shown to modulate both vesicle release and cargo sorting. In the context of rAAV production, increased SMPD3 activity may enhance vesicle formation and trafficking, thereby contributing to the export of vesicle-associated rAAV particles. However, the observed sensitivity to exogenous ceramide suggests that tight regulation of sphingolipid metabolism is required, as excessive ceramide levels may disrupt membrane organization and impair productive rAAV secretion. Together, these findings support a role for SMPD3-mediated lipid remodeling in modulating rAAV egress pathways.

Taking all this into account, no substantial differences were observed in the full-to-empty capsid ratio across conditions. Standard TT yielded approximately 13% full particles, while CD63 overexpression showed a modest increase to ∼16%, and the remaining conditions were comparable to the control (∼13%) (Table S2). These results suggest that the genetic modifications primarily influence rAAV secretion rather than genome packaging efficiency.

Using a DoE-based MD, the optimal combination, co-expressing of VPS37B and SMPD3, achieved nearly 50% extracellular viral egress, demonstrating strong potential for process intensification. These findings provide a rational foundation for engineering HEK293 stable cell lines with integrated *smpd3* and *vps37b*, designed specifically to maximize exo-rAAV recovery in batch TT processes, thereby improving yield, simplifying downstream processing, and increasing manufacturing efficiency.

Together, this integrative strategy, combining EGE phenotypic discovery, quantitative proteomics, functional validation, and DoE-based optimization, establishes a generalizable framework for host-guided viral vector engineering. It demonstrates that rAAV production platforms can be rationally redesigned to favor exo-rAAV secretion in batch systems, enabling scalable manufacturing of high-potency vectors. This represents a decisive step toward next-generation rAAV bioprocesses that couple biological insight with engineering principles to support the growing clinical and commercial demand for affordable, high-quality gene therapy vectors.

### Conclusions

This study demonstrates that EGE is a promising strategy to enhance exo-rAAV9 secretion at lab scale, increasing viral yield and promoting viral egress. By integrating high-throughput quantitative proteomics with functional validation, we identified key host-cell pathways and molecular regulators associated with exo-rAAV secretion, vesicle trafficking, and lipid metabolism. Targeted modulation of these pathways, particularly through CD63, VPS37B, SMPD3, and SNAP47, enabled the enhancement of extracellular rAAV9 recovery in standard batch processes, achieving near 50% viral egress and around >21% of exo-rAAVs in the SN through DoE-based optimization. Importantly, this work translates key features of the EGE phenotype into batch-compatible engineering strategies that may help improve upstream process performance while reducing process complexity, media usage, and production time. In addition, the observed presence of exo-rAAVs highlights the potential of this platform for generating vectors with improved delivery characteristics. Overall, these findings provide insight into host-cell mechanisms involved in rAAV9 egress and establish a framework for further development of scalable rAAV9 and secreted rAAV9 manufacturing strategies.

## MATERIALS AND METHODS

### Mammalian cell line and culture conditions

The cell line used in this work is a serum-free suspension-adapted HEK293 cell line (HEK293SF-3F6) kindly provided by Dr. Amine Kamen from the National Research Council of Canada (NRC, Montreal, Canada). Cells were cultured in disposable polycarbonate 125 mL flasks with vent cap (Dow Corning, NY, USA) at 37°C, 5% of $CO_2$ and 85% RH at 130 rpm in an LT-X Kuhner shaker (LT-X Kuhner, Birsfelden, Switzerland).

Cell culture media was FreeStyle F17 Expression media (Gibco, Life Technologies, Thermo Fisher Scientific, San Jose, CA, USA) supplemented with 8 mM GlutaMAX (Gibco), 0.1% Pluronic F-68 Non-ionic surfactant (Gibco) and IGF-1 (91590C, Sigma-Aldrich) at a final concentration of 50 μg/L. When required according to planned experiments, culture media was supplemented with 2 mg/L ceramide (860052 P, Avanti, Sigma-Aldrich) dissolved in dimethyl sulfoxide 99% (DMSO; W387520, Sigma-Aldrich). Cell concentration and viability were determined using the NucleoCounterNC-3000 automatic cell counter (Chemometec, Allerod, Denmark) according to manufacturer's instructions.

### Plasmids

Plasmids used for triple transfection (TT) were pHelper, pGOI, and pRep2Cap9 and were kindly provided by Dr. Fatima Bosch from Center for Animal Biotechnology and Gene Therapy (CBATEG, UAB, Bellaterra, Spain). Plasmid pRep2Cap9 encodes the Rep proteins from AAV2, and the Cap proteins from AAV9. Plasmid pGOI (pcohSgsh) encodes for a therapeutic gene.[12] The pHelper plasmid codifies for the adenovirus functions necessary for rAAV replication and packaging, namely: E2A, E4, and VA RNA I and VA RNA II. Plasmids were produced by Plasmid Factory (Bielefeld, Germany) and stored at −20°C. For potency assays, pGOI coding for *egfp* gene was used, to monitor transduction. For transfection control, pMock plasmid was used. This plasmid, devoid of any

mammalian promoter or coding DNA sequence (CDS) was engineered by ligating the pGag:eGFP backbone. Plasmids pSNAP47 and pRab32 were generated in-house. Briefly, *snap47* and *rab32* genes (Gene ID: 116841 and 10981, respectively) were obtained as a gBlock at IDT (Integrated DNA Technologies, Leuven, Belgium). They were amplified by polymerase chain reaction (PCR) and products were checked by gel electrophoresis and then digested with EcoRI-HF (R3101S, New England Biolabs) and NotI-HF (R3189S, New England Biolabs) for pSNAP47 or EcoRI-HF and KpnI (ER0521, Thermo Fisher Scientific) for pRab32. Fragments were cloned into pGFP vector previously digested with the same mentioned restriction enzymes before using T4 DNA ligase (M0202S, New England Biolabs). The shRNAs were designed using small interfering RNA (siRNA) design tool by IDT. Here, they were obtained as single-stranded DNA (ssDNA) ultramer (IDT), flanked by regions with sequence complementarity to a backbone containing U6 promoter,[50] which was PCR amplified. The PCR fragment with the ssDNA were incubated with Hi-Fi Master Mix 2× (New England Biolabs) incubating 1 h at 50°C using a molar ratio of 1:5 or 1:10.

Plasmids, pCD63 and pSMPDL were obtained from GenScript. Shortly, NM_001286138.1 for SMPDL gene and NM_001257389.1 for CD63 gene were cloned into pcDNA3.1 +/C-(K)DYK plasmid. Plasmid pVPS37B was constructed by GenScript using cDNA (NC_000012.12) and cloned into pcDNA3.1 +/C-(K)DYK plasmid.

### rAAV production by TT

Transfections were carried out at a cell density of $2 \times 10^6$ cells/mL. DNA:PEI complexes were formed by adding PEI to plasmid DNA diluted in fresh culture media (10% of the total culture volume to be transfected) at a ratio of DNA:PEI 1:2 (w/w). This ratio is the optimal DNA:PEI transfection ratio optimized in previous works.[51,52] Transfection reagent PEIpro (Polyplus-transfection) was used. Briefly, the corresponding DNA mixture was diluted with supplemented culture media and vortexed for 10 s. Then PEI was added in 1:2 (w/w) DNA:PEI ratio and vortexed three times, incubated for 15 min at room temperature and then added to the cell culture. For the EGE method, medium replacement (MR) was performed at 48 hpt by centrifuging the cell culture at 300× g for 5 min. The SN was harvested, and the cell pellet was gently resuspended with fresh media. After that, re-transfection was performed according to previous TT methodology. All conditions were performed in triplicate. For proteomic analysis, cell culture samples were taken at 48, 72, and 96 hpt by centrifuging the culture at 1,000× g for 10 min. The SN was collected and cellular pellets were stored at −80°C. For rAAV9 production analysis, SN was collected at 72 hpt. For cell Lys collection, cells were treated with 1× cell lysis solution (500 mM Tris, 1% Triton X-100 (v/v), 20 mM MgCl2 at pH 7.5) and incubated at 37°C, 130 rpm, for 1 h. Lysate mixture was centrifuged at 4,000× g for 20 min and SN was collected as cell Lys fraction. All fractions were stored at −80°C until analysis was performed.

### Harvest of EVs

The harvesting protocol of EV was adapted from Schiller et al.[33] Briefly, the culture from a 20 mL shake flask was harvested and centrifuged at 300× g for 5 min and at 1,000× g for 10 min sequentially. The SN fraction was then centrifuged at 17,700 g for 1 h at 4°C. Then, the SN was centrifuged again at 100,000× g for 1.5 h at 4°C in a Beckman Optima L100P centrifuge (Beckman Coulter Inc., Brea, CA, USA). The final pellet was resuspended in 200 μL of supplemented F17 cell culture media. Samples were kept at −80°C. Centrifugations were performed for each experimental condition in triplicate.

### qPCR

For the determination of vg titer, DNase I (10104159001, Roche, Basel, Switzerland) was added to SN samples at 0.066 mg/mL in a DNase buffer (0.16 mM $CaCl_2$, 6.6 mM $MgCl_2$, 17.3 mM Tris-HCl, 0.066% Pluronic F68, pH 8.0) and incubated at 37°C for 16 h. Then, 4 μL of EDTA 30 mM (AM9260G, Invitrogen, Carlsbad, CA, USA) was then added to each tube at and incubated at 70°C for 30 min. Then, 5 μL of 2 mg/mL Proteinase K (EO0491, Thermo Fisher Scientific) was added and incubated at 55°C for 2 h followed by inactivation at 95°C, 15 min qPCR reaction was set up using a set of primers specific to a region within the gene of interest using iTaq Universal SYBR Green Supermix (1725124, Bio-Rad, Hercules, CA, USA) using the recommended thermocycling profile in a CFX384 Touch Real-Time PCR Detection System. To quantify the accumulated rAAV titer in the SN, Equation 1 was used. To quantify the rAAV accumulated titer in the whole cell culture, the cell Lys fraction, Equation 2 was used. The total accumulated rAAV in the SN was determined by adding the titer of SN fraction at harvest (96 hpt) to the titer of the harvested SN fraction 48 hpt. Similarly, the total accumulated rAAV in the cell Lys fraction was determined by adding the titer of cell Lys fraction at harvest (96 hpt) to the titer of the harvested SN fraction 48 hpt.

$$Acc.\ rAAV\ in\ SN\ (vg) = rAAV\ titer\ SN_{96hpt} \times V + rAAV\ titer\ in\ SN_{48hpt} \times V \quad \text{(Equation 1)}$$

$$Acc.\ rAAV\ in\ Lysate\ (vg) = rAAV\ titer\ Lys_{96hpt} \times V + rAAV\ titer\ in\ SN_{48hpt} \times V \quad \text{(Equation 2)}$$

To determine the rAAV egress rate, the proportion of rAAV present in the SN fraction relative to the total rAAV was calculated using Equation 3:

$$Egress\ rate\ (Esn)\ (\%) = \frac{rAAV\ titer\ in\ SN}{rAAV\ titer\ in\ Lysate} x\ 100 \quad \text{(Equation 3)}$$

### Free-rAAV and exo-rAAV purification

Supernatant was clarified from the cell culture by an initial centrifugation at 3,000× g for 10 min. The resulting SN was sequentially centrifuged at 10,000× g for 10 min and at 17,000× g for 10 min. To purify free rAAVs, a 13 mL aliquot of the clarified SN was subjected to

iodixanol density-gradient ultracentrifugation at 103,000× g for 1.5 h at 4°C using an SW-32Ti rotor in a Beckman Optima L100XP centrifuge (Beckman Coulter Inc., Brea, CA, USA). The discontinuous gradient consisted of four layers: 60%, 40%, 25%, and 15% iodixanol. Following ultracentrifugation, the 40% iodixanol fraction containing free rAAVs was recovered. Finally, to isolate exo-AAVs, a 30 mL volume of the initially clarified SN was ultracentrifuged at 100,000× g for 1 h at 4°C. The SN was then discarded, and the resulting pellet was resuspended in 200 μL of PBS. Both fractions were stored at −80°C until analysis was performed.

#### Cell cycle analysis

Freshly harvested cells were pelleted by centrifugation, rinsed, resuspended in PBS and normalized to $1 \times 10^6$ cells in 500 μL. Cells were fixed with cold ethanol (70%) for 2 h at −20°C. For cell cycle analysis, cells were washed in PBS twice and stained with propidium iodide (PI) solution (50 μg/mL PI, 200 μg/mL RNAse A, 0.1% Triton X-100 (v/v)) for 30 min at 37°C prior to data acquisition with CytoFLEX (Beckman Coulter Inc., Brea, CA, USA). Data were processed using FlowJo v.10 (BD Biosciences, San Jose, CA, USA).

#### Protein samples preparation for mass spectrometry analyses

Pellets of each tested condition were obtained by centrifugation of 500 μL of the cell culture at 1,000× g for 10 min at 4°C. Pellets were stored at −80°C. Protein extraction was performed using extraction buffer (100 mM Tris-HCl pH = 8.8, 2mM EDTA, 4% SDS, 100 mM DTT) of which 100 μL were added to the cell pellet of each condition. Samples were sonicated for 5 min and then boiled for another 5 min. Protein extracts from pellets samples were quantified with RC/DC Protein Assay (Bio-Rad, Hercules, CA, USA) and stored in −20°C until the tryptic digestion process. Protein digestion was performed as previously described.[53] Proteins were digested using sequencing grade trypsin (Promega, Madison, WI, USA) and the filter-assisted sample preparation technology (FASP, Expedeon, San Diego, CA, USA), and the resulting peptides were subjected to Tandem Mass Tag (TMT)-10 plex labeling (AB Sciex, Framingham, MA, USA), joined and desalted. A total of 150 μg from samples of each condition was diluted to a final concentration of 100 mM of triethylammonium bicarbonate (TEAB) labeled with TMT-10 plex according to the manufacturer. Protein samples were labeled by adding 41 μL of TMT isobaric tag diluted in anhydrous acetonitrile, followed by a 1 h-incubation step at room temperature. To quench the reaction, 5% hydroxylamine (8 μL per sample) was added, incubated 15 min at room temperature and mixed together followed by addition of TFA 1% to lower pH at 3. TMT-labeled samples were equally mixed. Pooled mix was purified using Oasis HLB C18 column (Waters, MA, USA). TMT-labeled mix was fractionated using high pH reversed-phase peptide fractionation kit (Thermo Scientific, San Jose, CA, USA) according to manufacturer's instructions into 5 fractions for further liquid chromatography-tandem mass spectrometry (LC-MS/MS) analysis.

#### LC-MS/MS analysis

The tryptic peptide mixtures were subjected to LC-MS/MS analysis on a nano-HPLC Easy nLC 1000 liquid chromatograph (Thermo Scientific, San Jose, CA, USA) coupled to a QExactive mass spectrometer (Thermo Scientific, San Jose, CA). Peptides were suspended in 0.1% formic acid, loaded onto a C18 reverse-phase trapping column (Acclaim PepMap100, 75 μm internal diameter, 3 μm particle size, and 2 cm length, Thermo Scientific), and separated on an analytical C18 nano-column (EASY-Spray column PepMap RSLC C18, 75 μm internal diameter, 3 mm particle size, and 50 cm length, Thermo Scientific), in a continuous gradient (8%–31% B in 240 min, 31%–90% B in 2 min, 90% B in 7 min, and 2% B in 30 min; where buffer A is 0.1% formic acid in HPLC grade $H_2O$ and buffer B is 100% ACN, 0.1% formic acid in HPLC grade $H_2O$). Spectra were acquired using full ion scan mode over the mass-to-charge (m/z) range 390–1,500, 70,000 FT-resolution was performed on the top 15 ions in each full MS scan using the data-dependent acquisition mode with 45 s dynamic exclusion enabled.

#### Protein identification and quantification

Protein identification was performed over the raw files using the SEQUEST HT algorithm integrated in the Proteome Discoverer 2.1 (Thermo Finnigan). MS/MS scans were matched against a human database (UniProtKB/Swiss-Prot 2019_10 Release).

For database searching, parameters were selected as follows: trypsin digestion with 2 maximum missed cleavage allowed, precursor mass tolerance of 800 ppm, and fragment mass tolerance of 0.02 Da. TMT-10 plex labeling at N-terminal and lysine (+229.62932 Da) as well as cysteine carbamidomethylation (+57.021 Da) were chosen as static modifications, whereas methionine oxidation (+15.994915 Da) was chosen as dynamic modification. The same MS/MS spectra collections were searched against inverted database constructed from the same target database. SEQUEST results were analyzed by the probability ratio method.[54] False discovery rate (FDR) for identified peptides was calculated in the inverted database search results using the refined method.[55]

Quantitative information of TMT reporter ions was extracted from MS/MS spectra for relative quantification of protein abundance to characterize dynamic protein expression profiles in the selected conditions.

#### Statistical analysis

For the comparative analysis of the protein abundance changes, we applied Weighted Scan-Peptide-Protein (WSPP) statistical workflow,[56] using SanXoT package.[57] It uses as an input a list of quantifications in the form of log2-ratios (for example a condition versus control sample) with their statistical weights and generates the standardized forms of the original variables computing the quantitative values expressed in units of standard deviation around the averages. The quantitative information is obtained from the spectra and used to quantify the peptides from which the spectra are produced and then, proteins that generate these peptides. In other words, the quantitative information is integrated from the spectrum level to the peptide level and then from the peptide level to the protein level.[58] These standardized variables, (Zq), express the quantitative values in units

of standard deviation.[56] For the protein functional analysis, SBT model[58] was used. This algorithm estimates weighted functional category averages (Zc) from the protein values by performing the protein to category integration. After the integration from spectra to peptide and peptide to protein, this integration represents a higher level, from protein to category. The integration allows the detection of changes in functional categories produced by the coordinated behavior of their proteins.[58] Together with each Zq and Zc, the corresponding FDR was calculated. Around 5% FDR was considered significant. Only proteins identified with at least 2 unique peptides and processes quantified with at least 5 proteins were considered for downstream analysis. This commonly applied threshold increases the reliability of protein/process identification by minimizing false positives that may arise from single-peptide matches or ambiguous peptide/protein assignments. The quantified proteins were functionally annotated using the GO database.[59,60] For further GO annotation, DAVID[61,62] was used to perform functional enrichment analysis. To help analyze and comprehend the data, the online software for reactions, proteins, and pathways analysis Reactome[63] and the STRING[64] interaction network database were used.

### Particle size measurement

DLS experiments were performed using a Zetasizer Nano ZS instrument (Malvern Instruments, Malvern, UK) with a He/Ne 633 nm laser at 173°. The hydrodynamic diameter, particle size distribution in volume, derived count rate (dCR) and polydispersity index (PDI) were calculated with cumulative fit correlation at 25°C and 0.887 cP or 2.448 cP for concentrated samples by ultracentrifugation, respectively. Briefly, 50 μL of sample was placed in disposable plastic cuvettes (UV-Cuvette micro, BRAND GMBH, Germany) followed by automated experimental data collection. Technical triplicates with 12 scans of 10 s were performed in each independent measurement.

Nanoparticle tracking analysis (NTA) was performed with a NanoSight LM20 device (NanoSight Ltd., Amesbury, UK) at the Institut de Ciència de Materials de Barcelona (ICMAB, CSIC, Campus UAB), equipped with a neutral density filter for total particle by light scattering. Data were analyzed with NanoSight NTA 3.2 software. Briefly, samples were injected being previously diluted 1:20 and three independent analyses were carried out. Three video recordings of 60 s length were made for each sample. Subsequently, particles were identified and tracked by their Brownian motion at room temperature. NTA software allowed determining the size and number of EVs.

### rAAV9 *in vitro* potency assay

HEK293 cells were seeded at a concentration of $1 \times 10^5$ cells/well in a 96-well plate and incubated for 1 h at 37°C until cells were adhered. Then, rAAV9 samples were normalized to $1.2 \times 10^{10}$ vg/mL and added to each well at different dilutions ranging from multiplicity of infection (MOI) 500–4,000 in triplicate. WT AdV2 was kindly provided by TherivaTM Biologics (Parets del Vallès, Barcelona, Spain) and used at a MOI of 30 to enhance rAAV transduction efficiency.[65] Cells were harvested 24 h post-transduction (hptd) and the percentage of GFP-positive cells was assessed using Cytoflex (Beckman Coulter Inc., Brea, CA, USA). Gating was manually adjusted with HEK293 non-transduced cells as a control. Samples to be analyzed were concentrated 2-fold before analysis. A total of 5,000 events were analyzed per sample at a flow rate of 70 μL/min. Results were analyzed with the CytExpert v.2.3 software. The transducing units (TUs) were calculated using the following expression (Equation 4):

$$Transducing\ units\ (TU\ /\ mL) = \frac{GFP\ x\ N\ x\ FD\ x\ 1000}{V} \quad \text{(Equation 4)}$$

where GFP is the number of GFP-positive cells per well, $N$ is the number of cells per well at the time of transduction (corresponding to $1 \times 10^5$ cells per well), FD is the fold dilution of vector sample used for transduction at different MOIs, V is the volume of diluted vector sample added into each well for transduction in microliters.[65,66]

### Total capsid determination by ELISA

rAAV capsid titers were determined by ELISA (RAAV Titration ELISA, cat#PRAAV9, PROGEN Biotechnik GmbH, Heidelberg, Germany) according to the manufacturer's instructions. Samples were serially diluted to fit the standard curve of reference control provided by the kit. The standard curve was generated with the standard provided kit using a second-order quadratic polynomial curve fit and sample concentrations were automatically interpolated from the standard curve. Absorbances were acquired at 450 nm (SPECTROstar Nano, Ortenberg, Germany). Concentration values were averaged across the dilutions that were within the adjusted absorbance range recommended by the vendor and the standard deviation calculated. A minimum of two and to up to three dilutions were used for each sample.

### Cryo-TEM

A 2–3 μL amount of sample was blotted onto holey carbon grids (Quantifoil Micro Tools, Groβloebichau, Germany and Micro to Nano, Haarlem, the Netherlands) previously glow discharged in a PELCO easiGlow glow discharger unit. The samples were subsequently plunged into liquid ethane at −180°C using a Leica EM GP cryo workstation and observed in a JEM-2011 electron microscope (JEOL Ltd., Tokyo, Japan) operating at 200 kV. During imaging, samples were maintained at −173°C, and pictures were taken using a CCD-multiscan camera (Gatan Inc., Pleasanton, CA, USA).

### Dot blot

For Dot Blot analysis, the extracellular fraction from each sample was loaded (50 μL) on a polyvinylidene fluoride (PVDF) membrane, air dried and incubated for 1 h in blocking buffer (1× PBS, 0.1% (v/v) Tween 20 with 5% (w/v) non-fat milk) followed by 1 h incubation at room temperature with the corresponding primary antibody at room temperature with gentle shaking. Primary antibodies used were rabbit anti-CD63 antibody (ab134045, Abcam UK, 1:1,000), mouse anti-CD81 antibody (ab79559, Abcam, UK, 1:1,000),

anti-CD9 (ab223052, Abcam, UK, 1:1000) and anti-VPS37B (390144, Santa Cruz Animal Health, 1:200). After primary incubation, a secondary incubation was performed using HRP-linked anti-rabbit (A3562, Sigma-Aldrich, St. Louis, MO, USA) antibody at 1:2,500 in 2.5% (w/v) non-fat dry milk 1× Tris-buffered saline (TBS) 0.1% (v/v) Tween 20 for 1 h at room temperature. Proteins were visualized using Clarity Western ECL Substrate solution (Bio-Rad, Hercules, CA, USA) using ChemiDoc MP Imaging System (Bio-Rad, Hercules, CA, USA). Images were inverted, background signal was subtracted, and integrated cell density was quantified. A standard curve using purified EVs of known concentration was run in parallel. The concentration of EVs in the samples was determined by interpolating its integrated density data in the standard curve. ImageJ software[67] was used for analysis.

#### Optimal combination of candidate genes by DoEs

To optimize the viral egress rate (Esn) and specific productivity ($q_p$), a DoE strategy specifically employing a Mixture Design was used to determine the optimal ratios of various plasmids (pSMPD3, pSNAP47, and pVPS37B) impacting these responses. The DoE responses were quantified using Equation 3 to calculate the viral egress rate (Esn; percentage of rAAV9 in the SN) and Equation 5 for the specific productivity in the cell Lys ($q_p$; $vg \cdot cell^{-1} \cdot day^{-1}$ in Lysate), where IVCD is the integral viable cell density.

$$Specific\ productivity\left(q_p\ vg\cdot cell^{-1}\cdot day^{-1}\right) = \frac{rAAV\ titer\ in\ SN\ or\ Lys\left(\frac{vg}{mL}\right)}{IVCD} \quad \text{(Equation 5)}$$

The impact of the different plasmids on each response was assessed by varying their proportions in the transfection mixture, ensuring that the combined total for each experimental run equaled 1, which was set at $9 \times 10^{10}$ copies/mL. The specific proportions and combinations for each plasmid are detailed in Table 1. For each experimental run, the proportions of each plasmid were calculated relative to their 100% concentrations (in μg/μL) and different combinations of the three genes were prepared. Overall, the MD mixture accounted for $9 \times 10^{10}$ copies/mL of plasmid DNA, and the three additional plasmids for rAAV production (pHelper, pGFP_ITR and pRep2-Cap9) represented $1.8 \times 10^{10}$ copies/mL to the total DNA concentration. To achieve a total DNA concentration of 1 μg/mL, pMock was used. Simplex experimental results were fitted to a polynomial model described as follows (Equation 6):

$$Y = \beta_0 + \sum_{i=1}^{k}\beta_i \cdot X_i + \sum_{i=1}^{k-1}\sum_{j=i+1}^{k}\beta_{ij}\cdot X_i \cdot X_j \quad \text{(Equation 6)}$$

where Y is the response variable under consideration (Esn or $q_p$), $\beta 0$ is the model intercept term, $\beta i$ is the linear coefficient, $\beta ii$ is the interaction coefficient, and the coded factors $Xi$ and $X\,j$ are the independent variables of study, and $k$ is the number of independent variables. Statistical analysis and graphs facilitating model interpretation were performed using the Design-Expert Software (Stat-Ease, Inc). The model coefficients were determined using type III partial sum of squares. This allows for isolation of each variable's effect in the presence of other variables (Table 1). The fit of the model was quantified using the coefficient of determination ($R^2$), and the lack-of-fit (LOF) test was employed to evaluate the difference between experimental results and the pure error of the fitted equations. The overall significance of the model was determined using ANOVA $F$ tests, with each coefficient's significance assessed via the corresponding $t$ test. The $p$ values of 0.05 and 0.1 were considered as statistically significant, corresponding to confidence levels of 95% and 90%, respectively.

#### Experimental design and statistical rationale

For the multiplexed quantitative proteomics experiment based on TMT-10 plex labeling, three conditions were tested in this study: Non-transfected growth condition, a condition following the standard transfection protocol for AAV9 batch production based on TT and transfected following the EGE protocol characterized by a complete fresh medium replacement (MR) and retransfection step at 48 hpt for AAV9 production. A detailed description of the steps followed to optimize the EGE protocol can be found in previous works by Cervera et al.[68] and Lavado-García et al.[10] Samples from each condition were taken at three different time points: 48, 72, and 96 hpt as illustrated in Figure 1A. The TMT-based isobaric labeling quantification was performed with three biological replicates for each condition and time point. All individual values were normalized by the value from a peptide pool from the non-transfected condition at 48 hpt, which was used as an internal control for the all the statistical analyses.

## DATA AND CODE AVAILABILITY

The mass spectrometry proteomics data have been deposited to the ProteomeXchange Consortium (http://proteomecentral.proteomexchange.org) via the PRIDE partner repository with the dataset identifier PXD037988.

## ACKNOWLEDGMENTS

The authors thank Dr. Amine Kamen (McGill University, Montreal, Canada) for providing the HEK293SF-3SF6. The support of Dr. Jose Amable Bernabé from the Institute of Material Science of Barcelona (ICMAB-CSIC, Barcelona, Spain) with particle tracking techniques and the help of Martí del Cabo from the Microscopy Service from the Autonomous University of Barcelona (Barcelona, Spain) in the performance of electron microscopy analysis are greatly appreciated. This study was supported by competitive grants from the Spanish Ministry of Economy and Competitiveness (MINECO) (BIO2015-67580-P, PGC2018-097019-B-I00) through the Carlos III Institute of Health-Fondo de Investigación Sanitaria (PRB3, PT17/0019/0003 ISCIII-SGEFI/FEDER) and by CIBERCV (CB16/11/00277). The CNIC is supported by the Ministerio de Ciencia, Innovación y Universidades and the Pro-CNIC Foundation, and is a Severo Ochoa Center of Excellence (SEV-2015-0505). The UAB research group is recognized as 2017 SGR 898 by Generalitat de Catalunya. This work was supported by Novo Nordisk Fonden NNF20CC0035580 and NNF20SA0066621. J.L.-G. is supported by NNF22OC0078741 and the Marie Skłodowska-Curie Actions (MSCA) Postdoctoral Fellowship 101105465.

## AUTHOR CONTRIBUTIONS

J.L.-G., conceptualization, experimentation, data curation, analysis, writing – original draft, review, and editing; L.B.-M., conceptualization, experimentation, data curation, analysis, and writing – original draft; C.R.-A. and I.J., experimentation; J.V., and F.G., supervision; F.G., supervision, review, and editing; L.C., conceptualization, supervision, review, and editing.

## DECLARATION OF INTERESTS

Part of the contents of this work is covered by a published patent "method for production of gene therapy vehicles in mammalian cells" EP24159714.5/WO2025180875A2.

## DECLARATION OF GENERATIVE AI AND AI-ASSISTED TECHNOLOGIES IN THE WRITING PROCESS

During the preparation of this work, the authors used ChatGPT in order to improve flow and clarity of the text. After using it, the authors reviewed and edited the content as needed and take full responsibility for the content of the published article.

## SUPPLEMENTAL INFORMATION

Supplemental information can be found online at https://doi.org/10.1016/j.omta.2026.201815.

## REFERENCES


1. Mingozzi, F., and High, K.A. (2013). Immune responses to AAV vectors: overcoming barriers to successful gene therapy. Blood *122*, 23–36. https://doi.org/10.1182/BLOOD-2013-01-306647.
2. Zhong, L., Li, B., Mah, C.S., Govindasamy, L., Agbandje-McKenna, M., Cooper, M., Herzog, R.W., Zolotukhin, I., Warrington, K.H., Weigel-Van Aken, K.A., et al. (2008). Next generation of adeno-associated virus 2 vectors: Point mutations in tyrosines lead to high-efficiency transduction at lower doses. Proc. Natl. Acad. Sci. USA *105*, 7827–7832.
3. Bartel, M.A., Weinstein, J.R., and Schaffer, D.V. (2012). Directed evolution of novel adeno-associated viruses for therapeutic gene delivery. Gene Ther. *19*, 694–700. https://doi.org/10.1038/gt.2012.20.
4. Cabanes-Creus, M., Navarro, R.G., Zhu, E., Baltazar, G., Liao, S.H.Y., Drouyer, M., Amaya, A.K., Scott, S., Nguyen, L.H., Westhaus, A., et al. (2022). Novel human liver-tropic AAV variants define transferable domains that markedly enhance the human tropism of AAV7 and AAV8. Mol. Ther. Methods Clin. Dev. *24*, 88–101. https://doi.org/10.1016/J.OMTM.2021.11.011.
5. Grieger, J.C., Soltys, S.M., and Samulski, R.J. (2016). Production of recombinant adeno-associated virus vectors using suspension HEK293 cells and continuous harvest of vector from the culture media for GMP FIX and FLT1 clinical vector. Mol. Ther. *24*, 287–297. https://doi.org/10.1038/mt.2015.187.
6. Kuzmin, D.A., Shutova, M.V., Johnston, N.R., Smith, O.P., Fedorin, V.V., Kukushkin, Y.S., van der Loo, J.C.M., and Johnstone, E.C. (2021). The clinical landscape for AAV gene therapies. Nat. Rev. Drug Discov. *20*, 173–174. https://doi.org/10.1038/d41573-021-00017-7.
7. Lavado-García, J., Pérez-Rubio, P., Cervera, L., and Gòdia, F. (2022). The cell density effect in animal cell-based bioprocessing: Questions, insights and perspectives. Biotechnol. Adv. *60*, 108017. https://doi.org/10.1016/J.BIOTECHADV.2022.108017.
8. Legmann, R. (2020). Transient transfection at large scale for clinical AAV9 vector manufacturing. Cytotherapy *22*, S151. https://doi.org/10.1016/J.JCYT.2020.03.312.
9. Clément, N., and Grieger, J.C. (2016). Manufacturing of recombinant adeno-associated viral vectors for clinical trials. Mol. Ther. Methods Clin. Dev. *3*, 16002. https://doi.org/10.1038/mtm.2016.2.
10. Lavado-García, J., Cervera, L., and Gòdia, F. (2020). An alternative perfusion approach for the intensification of virus-like particle production in HEK293 cultures. Front. Bioeng. Biotechnol. *8*, 617. https://doi.org/10.3389/FBIOE.2020.00617.
11. Fuenmayor, J., Cervera, L., Gòdia, F., and Kamen, A. (2019). Extended gene expression for Gag VLP production achieved at bioreactor scale. J. Chem. Technol. Biotechnol. *94*, 302–308. https://doi.org/10.1002/jctb.5777.
12. Casablancas, F.G., Tubert, M.F.B., Martínez, M.G., Gracia, L.C., Madrenas, X.L., Laplana, M.M., and Granados, S.G. (2019). Methods for the manufacture of recombinant AAVS. https://patents.google.com/patent/WO2023232922A1/enw.
13. Henry, O., Perrier, M., and Kamen, A. (2005). Metabolic flux analysis of HEK-293 cells in perfusion cultures for the production of adenoviral vectors. Metab. Eng. *7*, 467–476. https://doi.org/10.1016/J.YMBEN.2005.08.002.
14. Vandenberghe, L.H., Xiao, R., Lock, M., Lin, J., Korn, M., and Wilson, J.M. (2010). Efficient serotype-dependent release of functional vector into the culture medium during adeno-associated virus manufacturing. Hum. Gene Ther. *21*, 1251–1257. https://doi.org/10.1089/hum.2010.107.
15. Lock, M., Alvira, M., Vandenberghe, L.H., Samanta, A., Toelen, J., Debyser, Z., and Wilson, J.M. (2010). Rapid, Simple, and Versatile Manufacturing of Recombinant Adeno-Associated Viral Vectors at Scale. Hum. Gene Ther. *21*, 1259–1271. https://doi.org/10.1089/HUM.2010.055.
16. Maguire, C.A., Balaj, L., Sivaraman, S., Crommentuijn, M.H.W., Ericsson, M., Mincheva-Nilsson, L., Baranov, V., Gianni, D., Tannous, B.A., Sena-Esteves, M., et al. (2012). Microvesicle-associated AAV vector as a novel gene delivery system. Mol. Ther. *20*, 960–971. https://doi.org/10.1038/mt.2011.303.
17. Orefice, N.S., Souchet, B., Braudeau, J., Alves, S., Piguet, F., Collaud, F., Ronzitti, G., Tada, S., Hantraye, P., Mingozzi, F., et al. (2019). Real-Time Monitoring of Exosome Enveloped-AAV Spreading by Endomicroscopy Approach: A New Tool for Gene Delivery in the Brain. Mol. Ther. Methods Clin. Dev. *14*, 237–251. https://doi.org/10.1016/j.omtm.2019.06.005.
18. Hudry, E., Martin, C., Gandhi, S., György, B., Scheffer, D.I., Mu, D., Merkel, S.F., Mingozzi, F., Fitzpatrick, Z., Dimant, H., et al. (2016). Exosome-associated AAV vector as a robust and convenient neuroscience tool. Gene Ther. *23*, 380–392. https://doi.org/10.1038/GT.2016.11.
19. Molina, E., Tejero, M., Duzenli, O.F., Kuoch, H., Caine, C., Krotova, K., Paulaitis, M., and Aslanidi, G. (2024). Insights in AAV-mediated antigen-specific immunity and a strategy for AAV vaccine dose reduction through AAV-extracellular vesicle association. Mol. Ther. Methods Clin. Dev. *32*, 101358. https://doi.org/10.1016/j.omtm.2024.101358.
20. Liu, B., Li, Z., Huang, S., Yan, B., He, S., Chen, F., and Liang, Y. (2021). AAV-Containing Exosomes as a Novel Vector for Improved Gene Delivery to Lung Cancer Cells. Front. Cell Dev. Biol. *9*, 707607. https://doi.org/10.3389/FCELL.2021.707607/PDF.
21. Meliani, A., Boisgerault, F., Fitzpatrick, Z., Marmier, S., Leborgne, C., Collaud, F., Simon Sola, M., Charles, S., Ronzitti, G., Vignaud, A., et al. (2017). Enhanced liver gene transfer and evasion of preexisting humoral immunity with exosome-enveloped AAV vectors. Blood Adv. *1*, 2019–2031. https://doi.org/10.1182/BLOODADVANCES.2017010181.
22. Issa, S.S., Shaimardanova, A.A., Solovyeva, V.V., and Rizvanov, A.A. (2023). Various AAV Serotypes and Their Applications in Gene Therapy: An Overview. Cells *12*, 785. https://doi.org/10.3390/cells12050785.
23. Lavado-García, J., Jorge, I., Cervera, L., Vázquez, J., and Gòdia, F. (2020). Multiplexed Quantitative Proteomic Analysis of HEK293 Provides Insights into Molecular Changes Associated with the Cell Density Effect, Transient Transfection, and Virus-Like Particle Production. J. Proteome Res. *19*, 1085–1099. https://doi.org/10.1021/acs.jproteome.9b00601.
24. Millet, R., Jolinon, N., Nguyen, X.-N., Berger, G., Cimarelli, A., Greco, A., Bertrand, P., Odenthal, M., Büning, H., and Salvetti, A. (2015). Impact of the MRN Complex on Adeno-Associated Virus Integration and Replication during Coinfection with Herpes Simplex Virus 1. J. Virol. *89*, 6824–6834. https://doi.org/10.1128/JVI.00171-15.
25. Schwartz, R.A., Palacios, J.A., Cassell, G.D., Adam, S., Giacca, M., and Weitzman, M.D. (2007). The Mre11/Rad50/Nbs1 complex limits adeno-associated virus transduction and replication. J. Virol. *81*, 12936–12945. https://doi.org/10.1128/JVI.01523-07.
26. Lavado-García, J., González-Domínguez, I., Cervera, L., Jorge, I., Vázquez, J., and Gòdia, F. (2020). Molecular Characterization of the Coproduced Extracellular Vesicles in HEK293 during Virus-Like Particle Production. J. Proteome Res. *19*, 4516–4532. https://doi.org/10.1021/acs.jproteome.0c00581.
27. Colombo, M., Raposo, G., and Théry, C. (2014). Biogenesis, Secretion, and Intercellular Interactions of Exosomes and Other Extracellular Vesicles. Annu. Rev. Cell Dev. Biol. *30*, 255–289. https://doi.org/10.1146/annurev-cellbio-101512-122326.
28. Kolmus, K., Erdenebat, P., Szymańska, E., Stewig, B., Goryca, K., Derezińska-Wołek, E., Szumera-Ciećkiewicz, A., Brewińska-Olchowik, M., Piwocka, K., Prochorec-Sobieszek, M., et al. (2021). Concurrent depletion of Vps37 proteins evokes ESCRT-I destabilization and profound cellular stress responses. J. Cell Sci. *134*, jcs250951. https://doi.org/10.1242/JCS.250951.

29. Trajkovic, K., Hsu, C., Chiantia, S., Rajendran, L., Wenzel, D., Wieland, F., Schwille, P., Brügger, B., and Simons, M. (2008). Ceramide Triggers Budding of Exosome Vesicles into Multivesicular Endosomes. Science *319*, 1244–1247. https://doi.org/10.1126/science.1153124.

30. Wei, D., Zhan, W., Gao, Y., Huang, L., Gong, R., Wang, W., Zhang, R., Wu, Y., Gao, S., and Kang, T. (2020). RAB31 marks and controls an ESCRT-independent exosome pathway. Cell Res. *31*, 157–177. https://doi.org/10.1038/s41422-020-00409-1.

31. Alenquer, M., Amorim, M.J., Graham, S., and Modis, Y. (2015). Exosome Biogenesis, Regulation, and Function in Viral Infection. Viruses *7*, 5066–5083. https://doi.org/10.3390/v7092862.

32. Takahashi, A., Okada, R., Nagao, K., Kawamata, Y., Hanyu, A., Yoshimoto, S., Takasugi, M., Watanabe, S., Kanemaki, M.T., Obuse, C., and Hara, E. (2017). Exosomes maintain cellular homeostasis by excreting harmful DNA from cells. Nat. Commun. *8*, 15287. https://doi.org/10.1038/ncomms15287.

33. Schiller, L.T., Lemus-Diaz, N., Rinaldi Ferreira, R., Böker, K.O., and Gruber, J. (2018). Enhanced Production of Exosome-Associated AAV by Overexpression of the Tetraspanin CD9. Mol. Ther. Methods Clin. Dev. *9*, 278–287. https://doi.org/10.1016/j.omtm.2018.03.008.

34. Sen, D., Balakrishnan, B., and Jayandharan, G.R. (2014). Cellular unfolded protein response against viruses used in gene therapy. Front. Microbiol. *5*, 91852. https://doi.org/10.3389/FMICB.2014.00250/FULL.

35. Wang, Y., Fu, Q., Lee, Y.S., Sha, S., and Yoon, S. (2023). Transcriptomic features reveal molecular signatures associated with recombinant adeno-associated virus production in HEK293 cells. Biotechnol. Prog. *39*, e3346. https://doi.org/10.1002/BTPR.3346.

36. Aponte-Ubillus, J.J., Barajas, D., Sterling, H., Aghajanirefah, A., Bardliving, C., Peltier, J., Shamlou, P., Roy, M., and Gold, D. (2020). Proteome profiling and vector yield optimization in a recombinant adeno-associated virus-producing yeast model. Microbiologyopen *9*, e1136. https://doi.org/10.1002/MBO3.1136.

37. Catalán-Tatjer, D., Tzimou, K., Nielsen, L.K., and Lavado-García, J. (2024). Unravelling the essential elements for recombinant adeno-associated virus (rAAV) production in animal cell-based platforms. Biotechnol. Adv. *73*, 108370. https://doi.org/10.1016/J.BIOTECHADV.2024.108370.

38. Ben-Israel, H., and Kleinberger, T. (2002). Adenovirus and cell cycle control. Front. Biosci. *7*, d1369–d1395. https://doi.org/10.2741/BEN.

39. Hoad, M., Roby, J.A., and Forwood, J.K. (2021). Structural characterization of the porcine adeno-associated virus Po1 capsid protein binding to the nuclear trafficking protein importin alpha. FEBS Lett. *595*, 2793–2804. https://doi.org/10.1002/1873-3468.14209.

40. Johnson, J.S., Li, C., DiPrimio, N., Weinberg, M.S., McCown, T.J., and Samulski, R.J. (2010). Mutagenesis of adeno-associated virus type 2 capsid protein VP1 uncovers new roles for basic amino acids in trafficking and cell-specific transduction. J. Virol. *84*, 8888–8902. https://doi.org/10.1128/JVI.00687-10.

41. Pols, M.S., and Klumperman, J. (2009). Trafficking and function of the tetraspanin CD63. Exp. Cell Res. *315*, 1584–1592. https://doi.org/10.1016/j.yexcr.2008.09.020.

42. Van Niel, G., D'Angelo, G., and Raposo, G. (2018). Shedding light on the cell biology of extracellular vesicles. Nat. Rev. Mol. Cell Biol. *19*, 213–228. https://doi.org/10.1038/nrm.2017.125.

43. György, B., Sage, C., Indzhykulian, A.A., Scheffer, D.I., Brisson, A.R., Tan, S., Wu, X., Volak, A., Mu, D., Tamvakologos, P.I., et al. (2017). Rescue of Hearing by Gene Delivery to Inner-Ear Hair Cells Using Exosome-Associated AAV. Mol. Ther. *25*, 379–391. https://doi.org/10.1016/j.ymthe.2016.12.010.

44. Henne, W.M., Buchkovich, N.J., and Emr, S.D. (2011). The ESCRT pathway. Dev. Cell *21*, 77–91. https://doi.org/10.1016/j.devcel.2011.05.015.

45. Vietri, M., Radulovic, M., and Stenmark, H. (2020). The many functions of ESCRTs. Nat. Rev. Mol. Cell Biol. *21*, 25–42. https://doi.org/10.1038/s41580-019-0177-4.

46. Hurley, J.H. (2015). ESCRTs are everywhere. EMBO J. *34*, 2398–2407. https://doi.org/10.15252/embj.201592484.

47. Jurado, S., Goswami, D., Zhang, Y., Molina, A.J.M., Südhof, T.C., and Malenka, R.C. (2013). LTP Requires a Unique Postsynaptic SNARE Fusion Machinery. Neuron *77*, 542–558. https://doi.org/10.1016/j.neuron.2012.11.029.

48. Holt, M., Varoqueaux, F., Wiederhold, K., Takamori, S., Urlaub, H., Fasshauer, D., and Jahn, R. (2006). Identification of SNAP-47, a novel Qbc-SNARE with ubiquitous expression. J. Biol. Chem. *281*, 17076–17083. https://doi.org/10.1074/jbc.M513838200.

49. Choezom, D., and Gross, J.C. (2022). Neutral sphingomyelinase 2 controls exosome secretion by counteracting V-ATPase-mediated endosome acidification. J. Cell Sci. *135*, jcs259324. https://doi.org/10.1242/jcs.259324.

50. Lavado-García, J., Díaz-Maneh, A., Canal-Paulí, N., Pérez-Rubio, P., Gòdia, F., and Cervera, L. (2021). Metabolic engineering of HEK293 cells to improve transient transfection and cell budding of HIV-1 virus-like particles. Biotechnol. Bioeng. *118*, 1649–1663. https://doi.org/10.1002/bit.27679.

51. González-Domínguez, I., Puente-Massaguer, E., Lavado-García, J., Cervera, L., and Gòdia, F. (2022). Micrometric DNA/PEI polyplexes correlate with higher transient gene expression yields in HEK 293 cells. N. Biotechnol. *68*, 87–96. https://doi.org/10.1016/J.NBT.2022.02.002.

52. González-Domínguez, I., Grimaldi, N., Cervera, L., Ventosa, N., and Gòdia, F. (2019). Impact of physicochemical properties of DNA/PEI complexes on transient transfection of mammalian cells. N. Biotechnol. *49*, 88–97. https://doi.org/10.1016/j.nbt.2018.09.005.

53. Wiśniewski, J.R., Zougman, A., Nagaraj, N., and Mann, M. (2009). Universal sample preparation method for proteome analysis. Nat. Methods *6*, 359–362. https://doi.org/10.1038/nmeth.1322.

54. Martínez-Bartolomé, S., Navarro, P., Martín-Maroto, F., López-Ferrer, D., Ramos-Fernández, A., Villar, M., García-Ruiz, J.P., and Vázquez, J. (2008). Properties of average score distributions of SEQUEST: the probability ratio method. Mol. Cell. Proteomics *7*, 1135–1145. https://doi.org/10.1074/mcp.M700239-MCP200.

55. Bonzon-Kulichenko, E., Garcia-Marques, F., Trevisan-Herraz, M., and Vázquez, J. (2015). Revisiting peptide identification by high-accuracy mass spectrometry: problems associated with the use of narrow mass precursor windows. J. Proteome Res. *14*, 700–710. https://doi.org/10.1021/pr5007284.

56. Navarro, P., Trevisan-Herraz, M., Bonzon-Kulichenko, E., Núñez, E., Martínez-Acedo, P., Pérez-Hernández, D., Jorge, I., Mesa, R., Calvo, E., Carrascal, M., et al. (2014). General statistical framework for quantitative proteomics by stable isotope labeling. J. Proteome Res. *13*, 1234–1247. https://doi.org/10.1021/pr4006958.

57. Trevisan-Herraz, M., Bagwan, N., García-Marqués, F., Rodriguez, J.M., Jorge, I., Ezkurdia, I., Bonzon-Kulichenko, E., and Vázquez, J. (2019). SanXoT: a modular and versatile package for the quantitative analysis of high-throughput proteomics experiments. Bioinformatics *35*, 1594–1596. https://doi.org/10.1093/bioinformatics/bty815.

58. García-Marqués, F., Trevisan-Herraz, M., Martínez-Martínez, S., Camafeita, E., Jorge, I., Lopez, J.A., Méndez-Barbero, N., Méndez-Ferrer, S., Del Pozo, M.A., Ibáñez, B., et al. (2016). A Novel Systems-Biology Algorithm for the Analysis of Coordinated Protein Responses Using Quantitative Proteomics. Mol. Cell. Proteomics *15*, 1740–1760. https://doi.org/10.1074/mcp.M115.055905.

59. Ashburner, M., Ball, C.A., Blake, J.A., Botstein, D., Butler, H., Cherry, J.M., Davis, A.P., Dolinski, K., Dwight, S.S., Eppig, J.T., et al. (2000). Gene Ontology: tool for the unification of biology. Nat. Genet. *25*, 25–29. https://doi.org/10.1038/75556.

60. The Gene Ontology Consortium (2017). Expansion of the Gene Ontology knowledgebase and resources. Nucleic Acids Res. *45*, D331–D338. https://doi.org/10.1093/nar/gkw1108.

61. Huang, D.W., Sherman, B.T., and Lempicki, R.A. (2009). Systematic and integrative analysis of large gene lists using DAVID bioinformatics resources. Nat. Protoc. *4*, 44–57. https://doi.org/10.1038/nprot.2008.211.

62. Huang, D.W., Sherman, B.T., and Lempicki, R.A. (2009). Bioinformatics enrichment tools: paths toward the comprehensive functional analysis of large gene lists. Nucleic Acids Res. *37*, 1–13. https://doi.org/10.1093/nar/gkn923.

63. Fabregat, A., Jupe, S., Matthews, L., Sidiropoulos, K., Gillespie, M., Garapati, P., Haw, R., Jassal, B., Korninger, F., May, B., et al. (2018). The Reactome Pathway Knowledgebase. Nucleic Acids Res. *46*, D649–D655. https://doi.org/10.1093/nar/gkx1132.

64. Szklarczyk, D., Morris, J.H., Cook, H., Kuhn, M., Wyder, S., Simonovic, M., Santos, A., Doncheva, N.T., Roth, A., Bork, P., et al. (2017). The STRING database in 2017: quality-controlled protein-protein association networks, made broadly accessible. Nucleic Acids Res. *45*, D362–D368. https://doi.org/10.1093/nar/gkw937.

65. François, A., Bouzelha, M., Lecomte, E., Broucque, F., Penaud-Budloo, M., Adjali, O., Moullier, P., Blouin, V., and Ayuso, E. (2018). Accurate Titration of Infectious AAV Particles Requires Measurement of Biologically Active Vector Genomes and Suitable Controls. Mol. Ther. Methods Clin. Dev. *10*, 223–236. https://doi.org/10.1016/j.omtm.2018.07.004.

66. Kutner, R.H., Zhang, X.Y., and Reiser, J. (2009). Production, concentration and titration of pseudotyped HIV-1-based lentiviral vectors. Nat. Protoc. *4*, 495–505. https://doi.org/10.1038/NPROT.2009.22.

67. Schneider, C.A., Rasband, W.S., and Eliceiri, K.W. (2012). NIH Image to ImageJ: 25 years of image analysis. Nat. Methods *9*, 671–675. https://doi.org/10.1038/nmeth.2089.

68. Cervera, L., Gutiérrez-Granados, S., Berrow, N.S., Segura, M.M., and Gòdia, F. (2015). Extended gene expression by medium exchange and repeated transient transfection for recombinant protein production enhancement. Biotechnol. Bioeng. *112*, 934–946. https://doi.org/10.1002/bit.25503.